Search for Dark Matter in Z+MET Events with the CMS Detector at $\sqrt{s} = 13\,\text{TeV}$

Sophie Kretzschmar

Bachelorarbeit in Physik

vorgelegt der

Fakultät für Mathematik, Informatik und Naturwissenschaften
der RWTH Aachen

im Januar 2016

angefertigt im
III. Physikalisches Institut A
bei
Prof. Dr. Thomas Hebbeker

Abstract

In this analysis, the dark matter production in proton-proton collisions at the Large Hadron Collider (LHC) at $\sqrt{s} = 13\,\text{TeV}$ with a Z boson and missing transverse energy based on simplified models is investigated. Different selection criteria are applied on data recorded by the CMS detector and Monte Carlo simulations of the standard model background and signal events in order to reduce the background and gain a good signal sensitivity for possible dark matter signals in the missing transverse energy distribution. The systematic uncertainties are estimated for the background in the signal regions.

No significant excess of data events is observed in the signal region. Model-independent 95% confidence level upper limits on cross sections for beyond standard model processes with Z+MET are calculated, as well as 95% confidence level upper limits on cross sections for different simplified model dark matter production scenarios. These limits are the first of their kind for a center of mass energy of 13 TeV.

Kurzdarstellung

In dieser Analyse wird die Erzeugung von Dunkle Materie mit einem Z-Boson und fehlender transversaler Energie in Proton-Proton Kollisionen am Large Hadron Collider (LHC) basierend auf vereinfachten Dunkle Materie Modellen untersucht. Sowohl auf Daten, die mit dem CMS Detektor aufgenommen wurden, als auch auf Monte Carlo Simulationen von Hintergrundereignissen des Standardmodells und Signalereignissen werden Auswahlkriterien angewandt, um den Hintergrund zu reduzieren und damit die Sensitivität für mögliche Dunkle Materie Ereignisse in der Verteilung der fehlenden transversalen Energie zu steigern. Die systematischen Unsicherheiten dieser Verteilung in den Signalregionen werden abgeschätzt. Kein signifikanter Überschuss an Daten wird beobachtet. Obere Ausschlussgrenzen mit 95% Konfidenzniveau werden sowohl für einen modellunabhängigen Wirkungsquerschnitt von Prozessen jenseits des Standardmodells mit Z-Boson und fehlender transversaler Energie berechnet, als auch für Wirkungsquerschnitte verschiedener Szenarien für die Erzeugung von Dunkler Materie. Diese Obergrenzen sind die ersten ihrer Art für Messungen mit einer Schwerpunktsenergie von 13 TeV.

Contents

Chapter 1

Introduction

1.1 Motivation

Dark matter is one of the great challenges to the modern physics today. In cosmology, strong evidence for this new kind of matter, which is only observable through its gravitational effects, is found (see section 1.2), but until now there is no indication for dark matter on a particle level. The standard model of particle physics (see section 1.3.2) does not contain a candidate which fulfills the requirements for a dark matter particle that would match to the observations in cosmology. It is therefore assumed that the dark matter particle is an extension to the standard model (see section 1.4).

1.2 Dark matter

In cosmology, there is strong evidence for a new form of matter, called "dark matter" [1]. First evidence was observed about 100 years ago by astronomers who tried to determine the masses and mass densities for astrophysical objects, like nebulae or galaxies. One of them was Fritz Zwicky who measured different velocities of objects in the Coma cluster in the 1930's [2]. He estimated the mass of this cluster based on the virial theorem and found out that there must be at least 400 times more mass than visible in the cluster.

Later in the 1960s, Vera Rubin started to observe different spiral galaxies and also measured the different velocities of the constituent stars in dependence of the distance r to the galactic center [3]. The results show a constant mean velocity $v(r)$ for radii r in the outer regions which is in contrast to the expectation of a decreasing rotational velocity, see fig. 1.1. This can be explained by a mass distribution in form of a halo in which the galaxy is embedded, rather than a centrally densed mass distribution which can be observed as visible matter.

Another way to compare luminous to dark matter is the gravitational lensing effect [1]: Light is deflected by the curvature of space-time caused by very massive

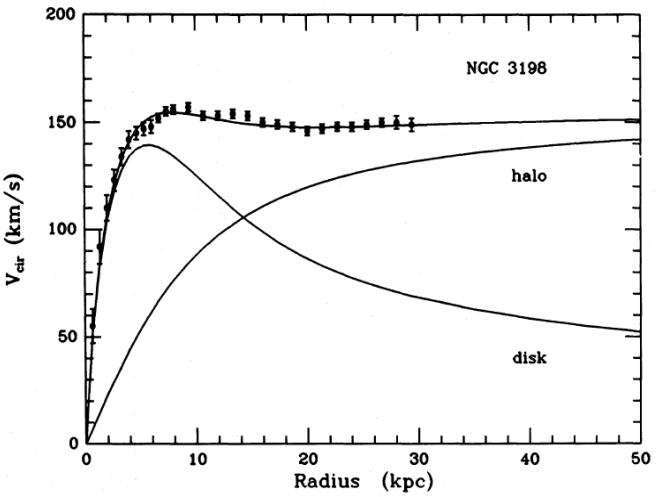

Figure 1.1: A graph of the rotational velocity of the constituents of the galaxy as a function of the distance to the galaxy core [4]. The expected curves are shown for a disk and halo mass distribution, and the measured data is shown as dots with error bars.

structures which is described in the theory of general relativity. In consequence, one observes multiple or arc-like pictures of objects that are located behind these massive structures. When an observable object, a massive structure acting as lens, and the observer are aligned (see fig. 1.2), one can observe a smeared ring as picture of the object with the lens in the middle, see fig. 1.3. Using the radius of this ring, one can calculate the mass of the structure that acts as the lens.

This is known as strong gravitational lensing effect, but the observation of the weak gravitational lensing effect is much more common [6]. In that case, one observes an elongation of background objects which is caused by a widely distributed mass in the range of focus. Based on this effect, maps of mass distributions can be made using statistical methods. A famous example is the bullet cluster picture, see fig. 1.3.

The visible to dark matter ratio can be also calculated for hot gas accumulations, so called intracluster medium. Multiple examples show a large discrepancy between the observed and expected mass [9–12].

Another evidence for dark matter can be found in observations of the cosmic microwave background (CMB). Interpreting these and other cosmological measurements within the standard model in cosmology, the ΛCDM model, one finds that only 5% of all matter is visible and 23% is dark matter [13].

In conclusion, one can say that there is strong astrophysical evidence for an invisible, but gravitationally interacting type of matter that is observed at different scales in the universe.

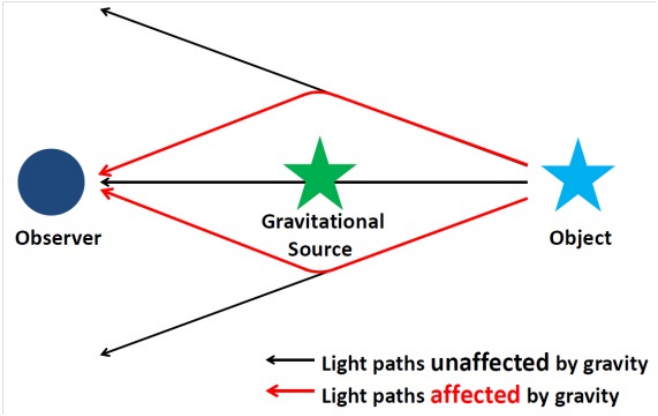

Figure 1.2: Sketch of the strong gravitational lensing effect [5]. The light of the object is deflected by the gravitational source. If the observer, the gravitational source, and the observer are aligned, the observer sees an arc-like smeared picture of the object.

Figure 1.3: Two pictures of gravitational lensing effect in space. One can reconstruct invisible mass, marked in blue, with the weak gravitational lensing effect (left, [7]) and see that it is not located at the visible matter (red). The strong gravitational lens effect (right, [8]) causes a ring shaped smearing of the luminous object behind the gravitational lens which is in the middle of the ring.

1.3 Particle physics

1.3.1 Natural units and cross sections

In particle physics, it is common to use the natural units convention which is given by $c = \hbar = 1$. This means all dimensions are converted into energy, so every unit is given in terms of electron volts (eV).

The cross section σ of a particle can be interpreted as its effective area for interaction processes, therefore, it has the dimensions of an area. Within the interpretation of an effective area, one can interpret the cross section also as a probability for these interaction processes to happen. The event rate $\dot{N}$ of a process with cross section σ is given by

$$\dot{N} = \mathscr{L}\sigma, \tag{1.1}$$

with the luminosity $\mathscr{L}$ in which the experimental settings are combined.

By integrating this equation over a range of time, one gets

$$N = \mathscr{L}_{\text{int}}\sigma, \tag{1.2}$$

with the number of interactions N and the integrated luminosity $\mathscr{L}_{\text{int}}$.

For collider searches, $\mathscr{L}$ is given by

$$\mathscr{L} = f\frac{n_b n_1 n_2}{4\pi\sigma_x\sigma_y}, \tag{1.3}$$

with the frequency of the bunch crossings f, the number of bunches n_b, the number of particles in the bunches n_i, and beam spread in the x-direction σ_x and in y-direction σ_y.

1.3.2 The standard model of particle physics

The standard model of particle physics is a very successful theory. Formally, it is a quantum field theory which can be used to calculate accurate predictions for high precision experiments, e.g. experiments at the LHC.

The standard model describes the particle physics processes as interactions of fields. Associated to these fields are their excitations appearing as elementary particles, namely the fermions with spin 1/2 which form matter, and bosons with integer spin that mediate the fundamental forces, the electromagnetic, weak and strong force. The fourth fundamental force, the gravitational force, is not included in the standard model of particle physics. For an overview of the elementary particles, see fig. 1.4.

The group of fermions contains the quarks and the leptons. The quarks have a charge of 2/3e (up, charm, top) or -1/3e (down, strange, bottom), and cannot be observed as free particles. They are confined into baryons which consist of three

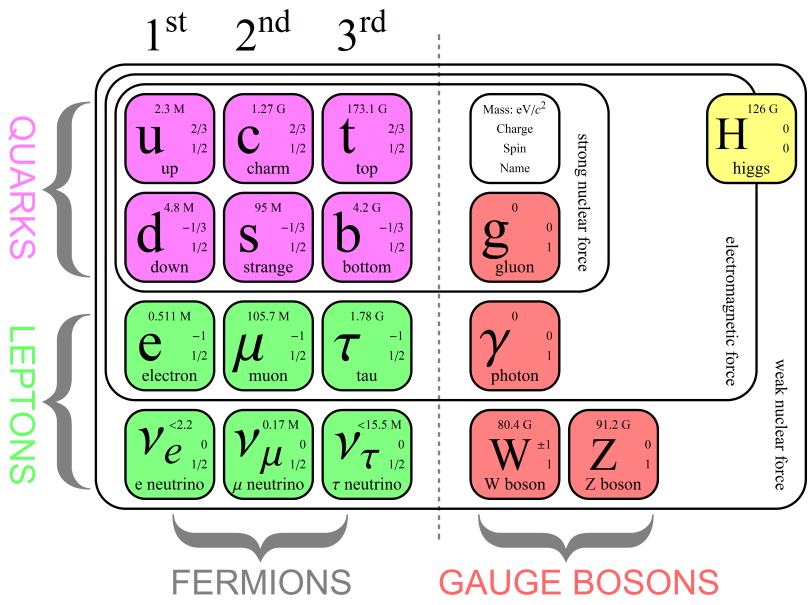

Figure 1.4: A collocation of all elementary particles of the standard model in particle physics [14].

quarks or antiquarks, or into mesons which consist of a quark and an antiquark. The group of leptons consists on one hand of the charged leptons, which are the electrons, muons and tauons, and on the other hand of the neutrinos each corresponding to a charged lepton - the electron-neutrino, the muon-neutrino and the tau-neutrino. All charged elementary particles have an antiparticle partner with the same mass but an opposite charge.

The electromagnetic force is mediated by the massless photon. It couples to the electrically charged particles, namely the quarks and the charged leptons. The theory of quantum electrodynamics (QED) describes these processes. Since the photon is massless, the range of the corresponding force is infinite.

The weak force is mediated by the Z and the $W^{\pm}$ bosons. They couple to all fermions and themselves, and the range of the weak force is limited since the Z and the $W^{\pm}$ have a mass. The electromagnetic and the weak force can be united within the electro-weak theory (EWT).

The gluons mediate the strong force. They couple to quarks and themselves, thus, the range is very short ranged due to their self-interaction, even though the gluons are massless. The strong force is the strongest known force, and the corresponding theory is called quantum chromodynamics (QCD).

With these particles and interactions in the theory, one cannot explain why the elementary particles have a non-vanishing mass which is then explained by the Higgs-mechanism. With the observation of the Higgs boson in 2012 [15], the associated particle to the Higgs field in the Higgs-mechanism, all particles of the

standard model have been observed.

However, there are still things which cannot be explained by the standard model. Open questions are for example, why the fundamental forces have such differences in strength, and what the cosmological dark matter is in the context of particle physics.

1.4 Particle dark matter

While there is strong evidence for dark matter in the universe at astrophysical scales, there is no evidence for dark matter on a particle level yet. Since all observable matter can be described as a composition of elementary particles, it is standing to reason to think that dark matter is made of elementary particles as well. Thus, one can derive the properties of dark matter particles from the observed phenomena in cosmology: Dark matter particles interact via gravitational force since the effects of dark matter are observed as additional mass. Due to the fact that dark matter is invisible, it does not interact via the electromagnetic force, but it is assumed to interact weakly. Due to measurements of the CMB (see section 1.2), it is assumed to be not baryonic.

In summary, the dark matter particle does not interact via electromagnetic, but via gravitational and weak force, thus, it should have a muss, but not carry an electrical charge.

The only possible candidate for dark matter in the standard model are neutrinos, but they cannot account for the large amount of dark matter alone because the relic density of neutrinos in the well established ΛCDM model is only about 1%, which is much less than the predicted 24% for dark matter [16]. Thus, there is no weakly interacting massive particle (WIMP) in the standard model, and one needs a theory beyond the standard model.

There are theories which provide candidates for such a dark matter particle. One example are the supersymmetric theories (SUSY) with their lightest stable particle, the neutralino $\tilde{\chi_1}^0$. This theory would unify the elementary forces naturally which means that at a certain energy scale the forces will have the same strength [16]. Therefore, measurements of dark matter on a particle level could be interpreted as the first hint to the existence of supersymmetric particles.

1.4.1 Detection of particle dark matter

In general, there are three ways to detect dark matter. One way is to detect particles which emerge out of annihilation processes of two dark matter particles [17, 18], e.g. γ-rays. This is referred to as indirect detection. Another possibility is the direct detection of dark matter by looking for scattering of dark matter particles with nuclei [19–21].The third detection possibility is to investigate the production of dark matter at colliders [22–26]. A sketch of these

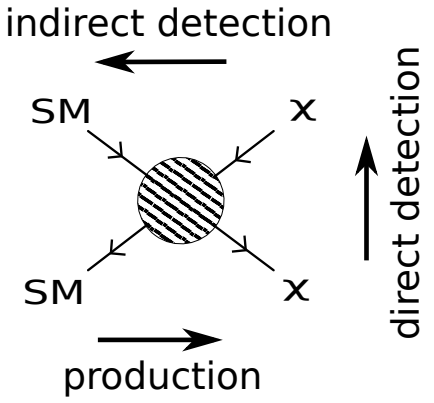

Figure 1.5: Considered ways of dark matter interaction. It is assumed that dark matter particles can annihilate with their antiparticles, scatter with standard model particles and be produced in collisions of standard model particles. Today's particle dark matter searches are based on these processes: The direct detection would be the measurement of recoiled standard model particles due to scattering processes with dark matter, the indirect detection would be the measurement of emerging standard model particles out of dark matter annihilations, and dark matter produced at colliders could be observed as additional signal to the standard model background.

detection possibilities can be found in fig. 1.5.

In this analysis, the dark matter production at the LHC is considered.

1.5 Simplified models and investigated processes

Simplified models for particle physics [27] are designed to give benchmark models with only few parameters that are directly related to the collider physics. In this framework, mediators that couple to quarks and the dark matter particles are assumed.

In this analysis, a simplified model for the process $pp \rightarrow Z + \text{mediator} \rightarrow \mu\mu\chi\chi$, is considered. This is in contrast to earlier analyses, where Effective Field Theory (EFT) approaches were performed. There, one considers the mediator to be so heavy that it decays in a negligible short time, so an effective contact-interaction between standard model and dark matter particles can be assumed. Within this framework, a similar analysis in the Z and missing transverse energy channel has been performed for 8 TeV [28]. There, the results are also discussed within an unparticle interpretation that would have the same signature as dark matter in the detector.

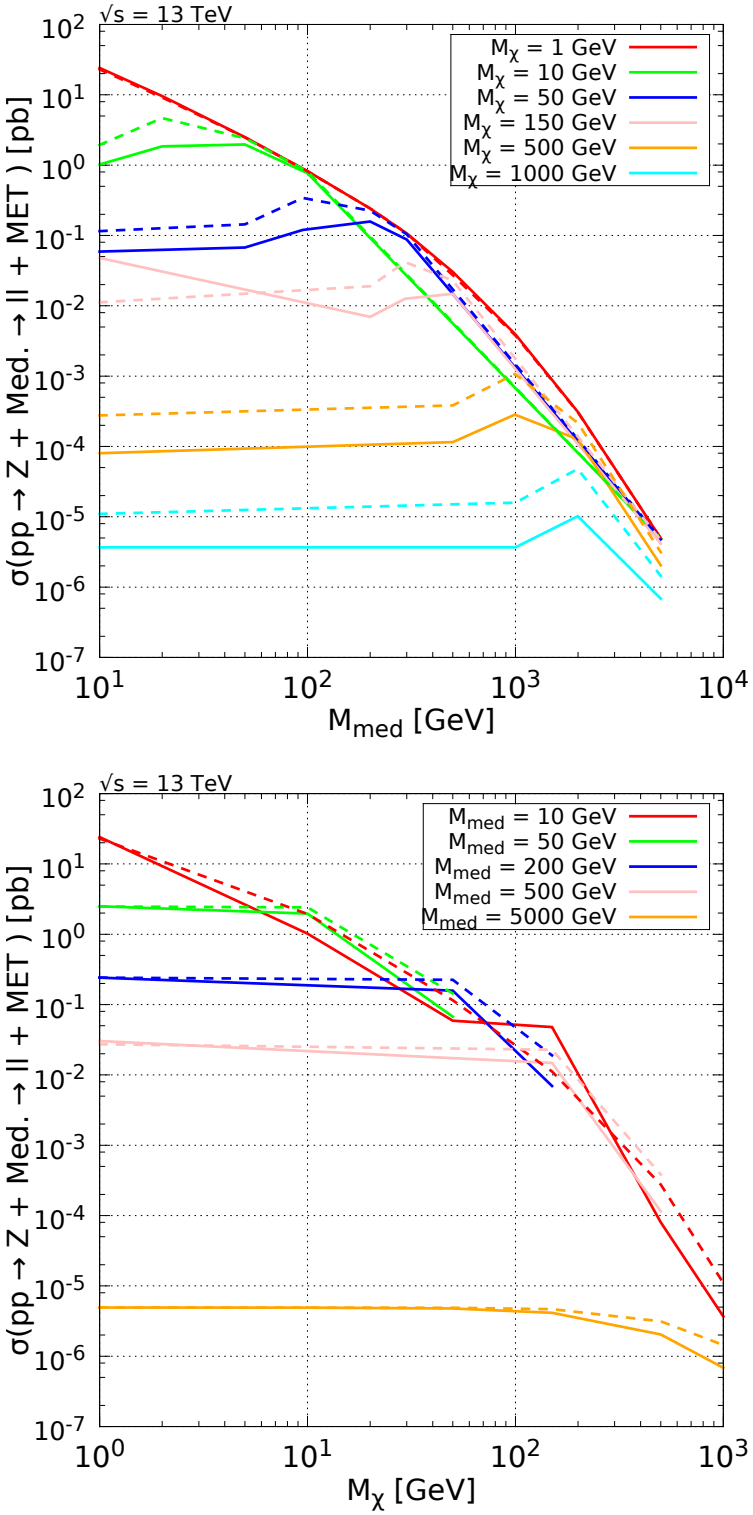

Figure 1.6: The cross sections of the dark matter production in dependence of the mediator mass (top) and dark matter mass (bottom). The solid lines denote the vector-coupling, the dashed the axial-vector coupling of the mediator to the dark matter particles χ.

Since the EFT approach is only valid for mediators with masses M_{med} higher than 2.5 TeV [29], simplified models are used for this analysis. The dark matter mass M_χ and the mediator mass M_{med} enter as parameters into these models. In this analysis, different dark matter scenarios with these masses and whether the mediator coupling is an axial-vector or vector coupling are used. The cross sections for the processes in dependence of the dark matter respectively mediator mass can be found in fig. 1.6.

1.6 The Experiment

1.6.1 The Large Hadron Collider

The Large Hadron Collider (LHC), a proton-proton and lead nuclei collider with a circumference of 27 km located near Geneva, is the most powerful particle physics experiment in the world [30]. About 2400 staff members at CERN (European Organization for Nuclear Research) and over 600 institutes and universities are participating in research in elementary particle physics there [31]. The protons are accelerated in opposite directions in beams, which contain up to 2508 bunches with $12 \cdot 10^{10}$ protons, and brought to collisions every every 25 ns at the four interaction points with a center of mass energy $\sqrt{s} = 13$ TeV. The largest four detectors of the LHC are located at these interaction points: The LHCb-Detector [32] which investigates the decay of B mesons, the ALICE Detector [33] which does research on quark-gluon plasma that is produced by lead-lead collisions, and the two general purpose detectors ATLAS [34] and CMS [35] which received a broad attention in media in 2012 for detecting the last piece of the standard model in particle physics - the Higgs boson.

1.6.2 The CMS detector

The Compact Muon Solenoid (CMS) [35] detector at the LHC consists of several detector layers and the solenoid that provides a magnetic field of 3.8 T. It is a general purpose detector and it is suited to detect the particles produced during the collisions within a broad geometrical acceptance. It can precisely measure the trajectories, energy and momentum of the detectable particles, and therefore provide a good measurement of the missing transverse energy which will be the physical observable in this analysis. Due to the approximately 10^9 proton-proton events per second that need to be filtered for the events of interest, a triggering system is implemented. Concerning the geometrical structure, the subdetector layers and the solenoid magnet are placed rotationally symmetric around the beam axis, and the endcap detectors are placed perpendicular to them to provide measurements of particles with flight direction nearly along beam axis. These constituents will be described in the following, for a sketch see fig. 1.7.

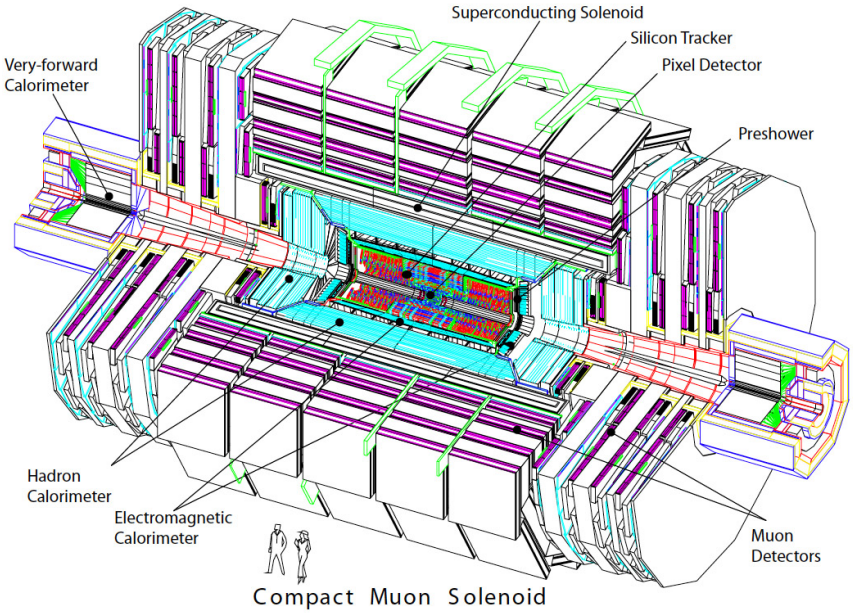

Figure 1.7: A sketch of the CMS detector [36]. Directly around the beam line, there is the tracker, and with increasing radii the ECAL, the HCAL, the solenoid and the muon detectors.

Coordinate system in the CMS detector

A particular coordinate system is commonly used for analysis using CMS data [35]. The transverse plane denotes the xy-direction, and with that e.g. the transverse momentum is defined as

$$\boldsymbol{p}_{\mathrm{T}} = p_x \boldsymbol{e}_x + p_y \boldsymbol{e}_y. \tag{1.4}$$

The bold print denotes the variables as vectors, here and in the following. The azimuthal angle ϕ is the angle to the x-axis which points to the center of the LHC, in the xy-plane, and the polar angle θ is defined as the angle to the beam axis in direction of the beam. Often, one uses the pseudorapidity η

$$\eta = -\ln \tan\left(\theta/2\right) \tag{1.5}$$

instead of the direct polar angle θ since differences in η are Lorentz-invariant under boosts in z-direction, so one can just add them up automatically taking relativistic kinematics into account. For the same reason, one often uses the rapidity

$$\Delta R = \sqrt{(\Delta\eta)^2 + (\Delta\phi)^2} \tag{1.6}$$

as a measure for the separation of particles within the detector.

For this analysis, the missing transverse energy (MET) $\boldsymbol{E}_{\mathrm{T}}^{\mathrm{miss}}$ is especially important. It is defined as

$$\boldsymbol{E}_{\mathrm{T}}^{\mathrm{miss}} = -\sum_{\mathrm{part.}} \boldsymbol{p}_T, \tag{1.7}$$

the negative sum over all measured particle momenta p_T, and describes the imbalance of the momenta in the plane perpendicular to the beams.

The magnet

The central element of the CMS detector is the solenoid magnet. It consists of a niobium-titanium (NbTi) coil, which is parallel aligned to the beam axis so that the magnetic field of up to 3.8 T is parallel to the proton beam, the barrel yokes, and endcap yokes. The barrel yokes and endcap yokes are massive iron elements that return and confine the magnetic flux. To provide such a high magnetic field a current of about 20 kA is needed, thus, to make use of the superconducting properties of NbTi, the coil is cooled with a Helium cooling-system. The magnet with the diameter of 6 m encloses the hadronic calorimeter, the electromagnetic calorimeter and the inner tracker systems. Between the yoke layers, there are the muon chambers - this compact structure gives one part of the detectors name.

Tracker detector

The tracker is the innermost detector of CMS and consist of the inner pixel detector and the strip detector. They are the nearest detectors to the interaction points of the protons and are designed to measure the trajectories of charged particles and identify the interaction vertices. For that purpose and due to the strong radiation load in this region, these detectors are chosen to be silicon detectors.

The inner tracker detector, the silicon pixel detector, consists of three cylindrical layers and two endcap discs at each side which precisely measure the trajectories of charged particles.

The outer tracker detector, the silicon strip detector, consists of three subsystems with 10 barrel layers and four endcap discs with several rings in addition which provide a coverage of $\eta = 2.5$.

Electromagnetic calorimeter

The electromagnetic calorimeter (ECAL) measures the energy of electrons and photons. When these particles enter the ECAL, their energy converts into scintillation light which can be used to calculate the deposited energy. The calorimeter is made of lead tungstate crystals ($PbWO_4$) which fulfill the requirements of the CMS detector: They are fast (nearly 80% of the light is emitted in 25ns), resistive to radiation and have a good energy resolution, e.g. for unconverted photons it

is about 1% [37]. The scintillator consists of the barrel part, where the light is collected by avalanche photodiodes (APDs), and the two endcaps with vacuum photodiodes (VPDs). The short radiation length of lead tungstate ($X_0 = 0.9\,\mathrm{cm}$) assures that most of the photons and electrons deposit their whole energy in the ECAL.

Hadronic calorimeter

The hadronic calorimeter (HCAL) measures the energy of hadrons. The geometry is organized in a way that there are as few gaps as possible to get a 'hermetic' detector. This is necessary because events with large missing transverse energy may lead to interesting new physics, thus, one wants to measure all the particles with the best possible resolution that emerged from the interaction point. The HCAL is divided into the barrel region (HB), the endcap region (HE), the outer calorimeter (HO) and the forward calorimeter (HF).

The HB is enclosed between the ECAL and the inner radius of the magnet coil and consists of several wedges in ϕ-direction which consist of brass absorber plates that are installed parallel to the beam axis. Between these absorber plates, there are plastic scintillators which provide long-term stability.

The HE is mounted on the preshower detector of the ECAL and provides an enlargement of the $|\eta|$ coverage up to the value of 3. It is also made of brass plates with slits in which the plastic scintillators are placed.

The HO is needed to detect showering hadrons in the region with $|\eta| > 1.3$, for that reason it is also called tail catcher. It consists of 5 rings which are placed between the solenoid coil, which is used as an additional absorber, and the muon chamber system. This overall tail catcher system increases the radiation length of the calorimeter system to at least $11.8\lambda_I$ (interaction length) which means that the very most of the hadrons deposit their whole energy there and are not able to pass it.

The HF consists of steel with quartz-fibers embedded. The quartz fibers are parallel to the beam axis, and half of them start at 22cm depth to distinguish between electrons and photons, and hadrons. Electrons and photons both leave a signal only in the fibers that are in the whole depth because they deposit their most energy in the first 22cm, and the hadrons leave signals in all fibers. The quartz fibers detect the Cerenkov radiation, thus they are sensitive to the electromagnetic part of the showers. Quartz is chosen as active material because of the harsh radiation environment. The HF extends the η range up to 5.2.

Muon detectors

The measurement of muon energy and momentum is a central task of the CMS detector. The muon system consists of two parts: The barrel and the endcap system. The barrel muon detector consists of 4 layers ("stations") of barrel drift

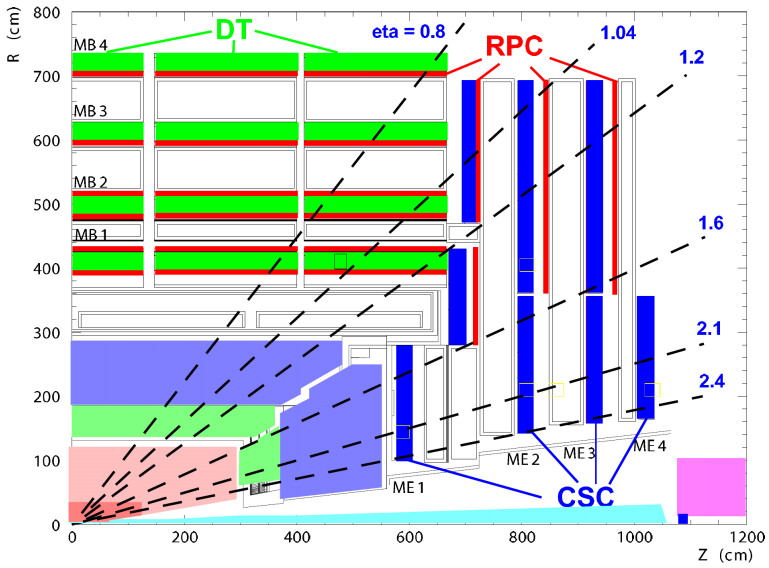

Figure 1.8: A sketch of the muon detectors in CMS [38]. The DTs, RPCs and CSCs are shown, as well as different η values. A muon detector coverage of up to $\eta = 2.4$ is provided.

tubes (DTs) which are 4cm wide tubes filled with a gas mixture (85% Ar and 15% CO_2). These stations are placed between the barrel yokes of the magnet. The DTs are appropriate here because the magnetic field is uniform and the muon rates are low. In the endcap region, cathode strip chambers (CSCs) are used since the muon rate is higher, and the magnetic field is not as homogeneous as in the barrel region.

Additionally, there are resistive plate chambers (RPCs) both in barrel and endcap region to provide a very good triggering system for muons over a large pseudorapidity range $|\eta| < 1.6$. All DTs, CSCs and RPCs are often colloquially referred to as the muon chambers. The overall muon detection system has a muon momentum resolution of 5% for muons with a transverse momentum of 1 TeV.

A sketch of the muon system can be found in fig. 1.8.

1.7 Monte Carlo simulation and computational setup

The protons which are brought to collision inside the CMS detector are composite particles, so the momentum of the initial state quarks is unknown since the total energy of the proton is distributed among its constituents. Using the standard model, theorists can calculate the interaction cross sections of the possible processes depending on the momentum and the elementary properties of the initial state particles. Thus, in order to obtain predictions of the standard model processes that happen at the collision points, Monte Carlo simulations utilizing the rules of the standard model in particle physics are performed. The programs that are designed to perform Monte Carlo simulations based on the standard model rules, are called generators. For this analysis, samples generated by MadGraph [39] and POWHEG [40] are used. With these Monte Carlo generators, events for certain final states can be simulated, and using these simulations the distributions of observables can be computed.

Since the detector is not ideal, the measurements depend on the resolution and geometrical properties of the detector. To take these effects into account, the Monte Carlo simulation of events is sent to a full detector simulation which uses the GEANT4 framework [41]. These simulated events then are used to estimate contributions of the standard model.

The number of events contributed by a process with cross section σ is given by (see section 1.3.1)

$$N = \mathscr{L}_{\text{int}}\sigma, \tag{1.8}$$

therefore, Monte Carlo simulations can be performed for a large amount of events and then reweighted by a factor f via

$$N_{\text{measured}} = \underbrace{\frac{\sigma\mathscr{L}_{\text{int}}}{N_{MC}}}_{=:f} N_{\text{MC}}, \tag{1.9}$$

with the number of measured data events N_{measured}, the number of generated Monte Carlo events N_{MC}, the cross section σ for the particular process, and the recorded integrated luminosity $\mathscr{L}_{\text{int}}$.

The analysis framework TAPAS [42] (short for 'Three A Physics Analysis Software'), which is based on the CMS data analysis software CMSSW [43] (CMS SoftWare), is used for both analysis and most of the plotting.

Chapter 2

Analysis

2.1 Overview of the analysis

The goal of this analysis is to design a selection which is sensitive for possible dark matter processes at the LHC. The missing transverse energy distribution is used for this search. The different dark matter scenarios are simulated using the well-established Monte Carlo technique. The standard model processes are modelled using Monte Carlo simulations as well to provide an estimate of their contribution (section 2.3). Requirements on the considered events are applied for data and simulation to lower the contributions of the standard model processes, but maintain the possible signal, and therefore increase the sensitivity for a possible dark matter signal (section 2.8). A pileup reweighting of the simulated background and signal is performed to account for effects of additional elastic scattering along the events of interest (section 2.6), and the systematic uncertainties on the background are estimated for the signal regions (section 2.9). Since there is no significant excess of data, upper limits on both model-independent and production cross sections for different dark matter scenarios are calculated (chapter 3).

2.2 Signature of the process

In this analysis, the dark matter production channel with a Z boson and missing transverse energy is investigated, see fig. 2.1.

It is assumed that a Z boson and a dark matter mediator emerge from the proton-proton collision. This mediator then decays into two dark matter particles which leave CMS undetected and result in a missing transverse energy. The Z boson decays into two muons. Thus, the final state of this process consists of two muons with $m_{\mu\mu} \approx m_Z$, and missing transverse energy.

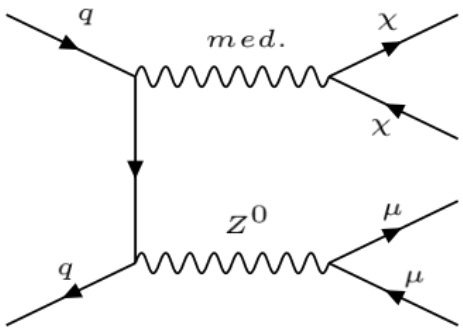

Figure 2.1: A Feynman diagram of the dark matter production in the Z+MET channel. A Z boson emerges from the proton-proton collision and recoils against a mediator which then decays into two dark matter particles that result in a missing transverse energy. The Z boson decays into two oppositely charged muons.

M_χ [GeV] / M_{med} [GeV]	1	10	50	150	500	1000
10	x	x	x	x	x	x
20	x	x				
50	x	x	x			
95			x			
100	x	x				
200	x		x	x		
295				x		
300	x		x			
500	x			x	x	
995	x				x	
1000	x					x
1995						x
2000	x				x	
5000	x	x	x	x	x	x

Table 2.1: The M_χ and M_{med} combinations that are available as Monte Carlo samples are denoted by 'x'. These samples are available for both axial-vector and vector coupling of the mediator to the dark matter.

2.3 Standard model backgrounds

The signature mentioned above is fulfilled by standard model processes, in the following denoted as standard model background. In data, it is not possible to distinguish between standard model background and the possible dark matter signal. Thus, to see if there are dark matter events, the background must be reduced. This is done by applying selection criteria on data and Monte Carlo simulation of background and signal which sort out events of background, but not of the signal. In the following, the standard model background processes will be described as well as properties to differentiate between them and the signal.

Since one is looking for muons which emerge out of a Z boson, every background process that contains a Z boson in the final state must be considered. The process known as Drell-Yan ($\gamma/Z \to \mu\mu$) satisfies this requirement, but since all particles in the final states are detectable, there will be small missing transverse energy only due to detector inefficiencies and mismeasurement. Additionally, the azimuthal angle between the missing transverse energy and the muon pair $\Delta\phi_{\mu\mu,\mathrm{MET}}$ is expected to be evenly distributed.

The ZZ background ($ZZ \to \mu\mu\nu\nu$) is an irreducible background, since it has the exact same kinematics as the dark matter signal.

The WZ background ($WZ \to \mu\mu l\nu_l$) has a neutrino in the final state which is a particle that cannot be detected. The third lepton can be used to set a veto requirement on these signatures of events to suppress the WZ background.

Another class of background processes are the backgrounds with no Z boson as mediator, colloquially referred to as non-resonant backgrounds. These contain two muons in the final state and missing transverse energy, but can significantly be reduced by the Z mass requirement discussed earlier since the muons originate from two different decays. These are the WW background ($WW \to \mu\nu\mu\nu$), the single-top background ($tW \to b\mu\nu\mu\nu$) and the top quark pair background ($t\bar{t} \to b\mu\nu b\mu\nu$).

The Monte Carlo samples for the standard model background and dark matter signal are listed in table 2.2 and table 2.1, respectively.

2.4 Data samples

The data samples are recorded by the CMS detector in 2015 during the Run D with an integrated luminosity $\mathscr{L}_{\mathrm{int}} = 1.3\,\mathrm{fb}^{-1}$. Only the data events with full functionality of the magnet and bunch spacing of 25 ns are used.

2.5 Muon selection

This analysis relies on precise measured muons, therefore, only events with two well reconstructed muons within the detector coverage of $|\eta| < 2.4$ are selected.

Sample	Generator	N_{gen}	σ in pb (pert. order)
DYJetsToLL_M-50	MadGraph	$1.8 \cdot 10^7$	6025.5 (NNLO)
DYJetsToLL_M-5to50_13TeV	MadGraph	$1.9 \cdot 10^7$	71310.0 (LO)
WZTo3LNu_13TeV	POWHEG	$2.0 \cdot 10^6$	4.42965 (NLO)
ZZTo2L2Nu_13TeV	POWHEG	$8.6 \cdot 10^6$	0.564 (NLO)
ST_tW_antitop_5f_inclusiveDecays	POWHEG	$1.0 \cdot 10^5$	35.6 (NNLO)
ST_tW_top_5f_inclusiveDecays	POWHEG	$1.0 \cdot 10^5$	35.6 (NNLO)
TTTo2L2Nu_13TeV	POWHEG	$5.0 \cdot 10^6$	87.31 (NNLO)
WWTo2L2Nu_13TeV	POWHEG	$2.0 \cdot 10^6$	12.178 (NNLO)
DarkMatter_MonoZToLL	MadGraph	$\approx 5.0 \cdot 10^4$	see section 1.5 (LO)

Table 2.2: List of the used Monte Carlo samples for background and signal samples. The respective Monte Carlo generator is given as well as the number of generated events N_{gen} and the corresponding cross sections [44]. For the dark matter samples, N_{gen} varies depending on the chosen scenario.

It has to be assured that the muons do not originate from secondary interactions or are cosmic muons. Thus, only events with two muons that fulfill the tightID criteria [45] are considered. Additionally, the muons must have an invariant mass consistent with the Z boson which is defined by $|m_Z - m_{\mu\mu}| < 10$ GeV.

To fulfill the tightID criteria, the muon has to be a global muon. That means that the muon is required to have a global track which consists of measurements in both the tracker system and the muon system. Additionally, the global-muon track fit has to have a χ^2/ndof better than 10. Next, there are muon detector and tracker requirements: The muon has to leave a signal in at least one muon chamber, which is included in this global-muon track fit, and there have to be at least two muon station measurements. The muon track in the tracker needs to have at least 1 pixel measurement and 6 tracker layer measurements to guarantee a good determination of the transverse momentum of the considered muon.

The muon has to come from a primary vertex, thus, there is a requirement on the measured track of the muon and the primary vertex position: The distance to the beam spot in the xy-plane d_{xy} has to be smaller than 2 mm, and in z-direction d_z smaller than 5 mm.

Furthermore, the muons are required to be isolated from hadronic activity. Thus, as an isolation requirement, the colloquially called Particle Flow Isolation ID (pfIsoID) criteria are required. To fulfill the requirements of this ID, only muons which present with a hadronic activity less than 12 % of the muon transverse momentum in a cone of $\Delta R = 0.4$ are selected [46].

These tightID and pfIsoID requirements are implemented in TAPAS with the requirements for the muon mentioned above, and used for the analysis as selection criteria on the muons.

As trigger, the double muon trigger with a p_{T} threshold value of 17(8) GeV

for the first (second) muon and very loose tracker isolation requirement is used. In order to avoid suffering from the trigger p_{T} threshold effects, both muons must have a transverse momentum greater than 20 GeV.

2.6 Pileup reweighting

The great amount of protons that are brought to collision with such high frequency (see section 1.6.1) leads to many additional soft interactions along the processes one is interested in. This effect is colloquially called pileup. In order to account for this effect, a certain pileup scenario is assumed during the production of the Monte Carlo samples. Since the real pileup scenario is different and not known until data is taken, a correction of the Monte Carlo samples has to be performed. The CMS detector measures the number of vertices N_{vertices} in an event. With this measured N_{vertices}, the simulated Monte Carlo events are reweighted using

$$\mathrm{weight}(N_{\mathrm{Vertices}}) = \frac{N_{\mathrm{Data}}(N_{\mathrm{Vertices}})}{N_{\mathrm{MC}}(N_{\mathrm{Vertices}})}, \tag{2.1}$$

so that the number of vertex distribution matches the distribution measured in data.

To do so, the number of vertices of the Monte Carlo simulations $N_{\mathrm{MC}}(N_{\mathrm{Vertices}})$ is known exactly since it is put into the MC simulation as a parameter, and the $N_{\mathrm{Data}}(N_{\mathrm{Vertices}})$ distribution can be calculated with CMSSW [47] using the measured instantaneous luminosity and the known total inelastic cross section for proton-proton collisions (73,1 mb [34]).

The distribution of the number of vertices before and after the reweighting can be found in fig. 2.2.

2.7 Missing transverse energy

The missing transverse energy of an event is given by

$$\mathbf{E}_T^{\mathrm{miss}} = -\sum \mathbf{p}_T, \tag{2.2}$$

while $\sum \mathbf{p}_T$ is the vector sum over the transverse momenta of every particle that was measured.

By applying corrections, one can correct the MET defined above for known effects like pileup, jet energy mismeasurement and xy-shift [48] following the recommendations issued by the CMS MET group. These corrections will be shortly described in the following.

Due to the pileup effect (section 2.6), there are more particles along the interaction of interest which also contribute to the MET, so there is a difference

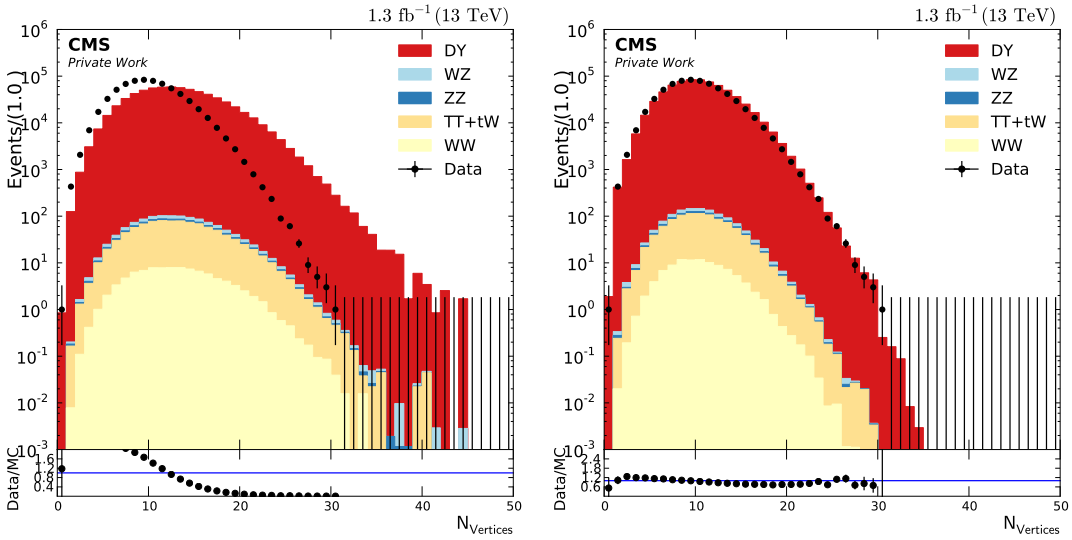

Figure 2.2: Comparison of the reconstructed number of vertices distribution of the Monte Carlo simulation before and after pileup reweighting. Only events that pass the event selection are considered. The data distribution is not changed.

between the measured MET by the detector and the MET produced in the interaction of interest. To correct for this MET difference one considers the particles from pileup to have mostly low $|\mathbf{p}_T|$, so they can be identified and removed from the event to achieve the MET only caused by the interaction of interest.

Jets arise from hard parton-parton interactions which leave a particle shower in the hadronic calorimeter. Due to the fact that the measurements of the energy of these clustered hadrons (in MC simulations often referred to as CaloJets) differ from the energy of the final state partons (in MC simulations often referred to as GenJets), one has to apply corrections for these jet measurements to take these effects into account [49].

The xy-shift correction is necessary because the MET is dependent on ϕ, which may be a consequence from detector effects or misplacement of the beam.

These corrections mentioned above are applied in the skimming process within TAPAS [42]/CMSSW [43].

2.8 Final event selection

Applying the selection criteria mentioned in section 2.5, and especially the requirement on the dimuon mass, the non-resonant backgrounds (top quark pair, WW and single top) are reduced. A plot of this dimuon mass distribution is shown in fig. 2.3.

The missing transverse energy of the Drell-Yan process is only due to detector

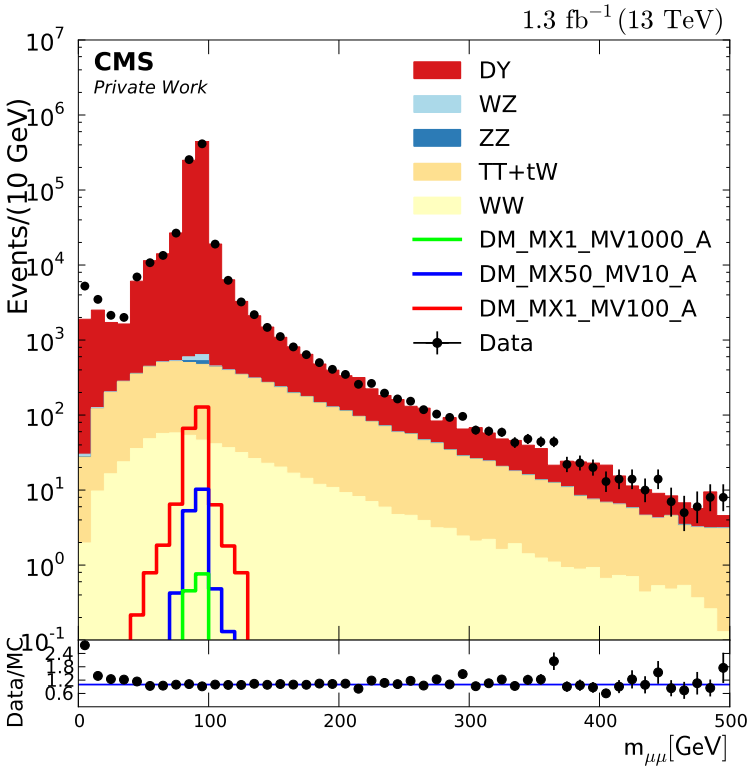

Figure 2.3: The invariant mass of the selected muon pair (see section 2.5). The Z resonance peak around 91 GeV is clearly visible. One can see that a selection criterion on the dimuon mass will reduce the background significantly, but not the signal.

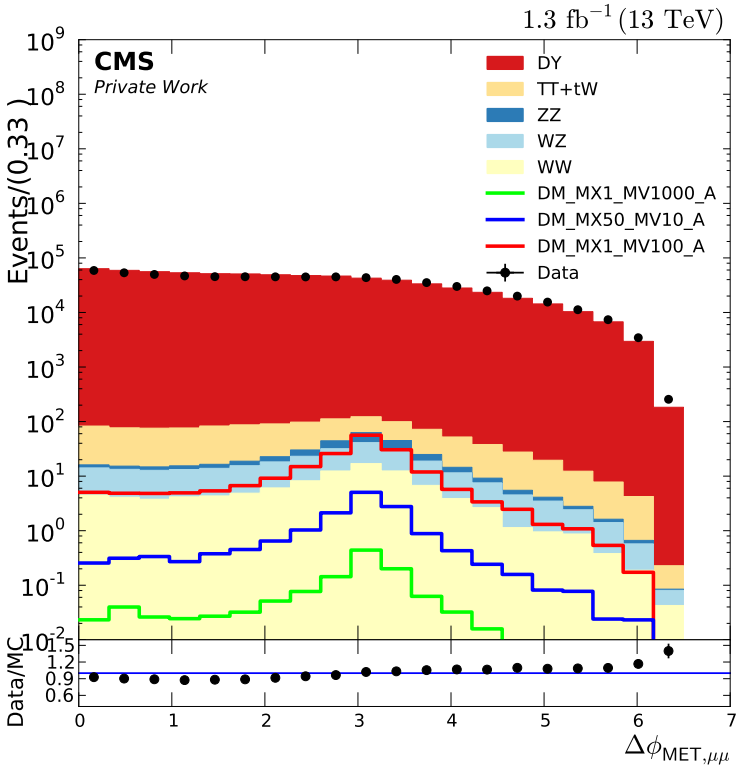

Figure 2.4: The $\Delta\phi_{\mathrm{MET},\mu\mu}$ distribution. The signal has a broad maximum at π, and the Drell-Yan distribution is very broad distributed, so as selection criterion with $2 < \Delta\phi_{\mathrm{MET},\mu\mu} < 4$ is demanded for the final selection. Thereby, the signal is reduced as well but not as much as the background.

effects (as mentioned in section 2.3) and the $\Delta\phi_{\mathrm{MET},\mu\mu}$ distribution is expected to be flat. Since the dark matter mediator is expected to recoil against the Z boson, the signal $\Delta\phi_{\mathrm{MET},\mu\mu}$ distribution is expected to be at maximum at π (fig. 2.4). For that reason, only events with $2 < \Delta\phi_{\mathrm{MET},\mu\mu} < 4$ are selected.

A summary of these requirements is shown in table 2.3, and an overview of these respective selection efficiencies are shown in fig. 2.5. The missing transverse energy distribution with three dark matter signals as benchmarks after applying these final selection criteria can be found in fig. 2.6.

2.9 Systematic uncertainties

Since the investigated distribution in this analysis is the MET distribution, the systematic uncertainties on the energy of every measured particle and on the

Variable	Requirement
muon ID	tightID (see section 2.5)
muon isolation	pfIsoID (see section 2.5)
$\lvert\eta_\mu\rvert$	< 2.4
N_{muons}	2
p_{T}^{μ}	> 20 GeV each
$\lvert M_{\mu\mu} - M_Z\rvert$	< 10 GeV
$\Delta\phi_{\mu\mu,\text{MET}}$	$2 < \Delta\phi_{\mu\mu,\text{MET}} < 4$

Table 2.3: Summarized selection criteria for the final event selection.

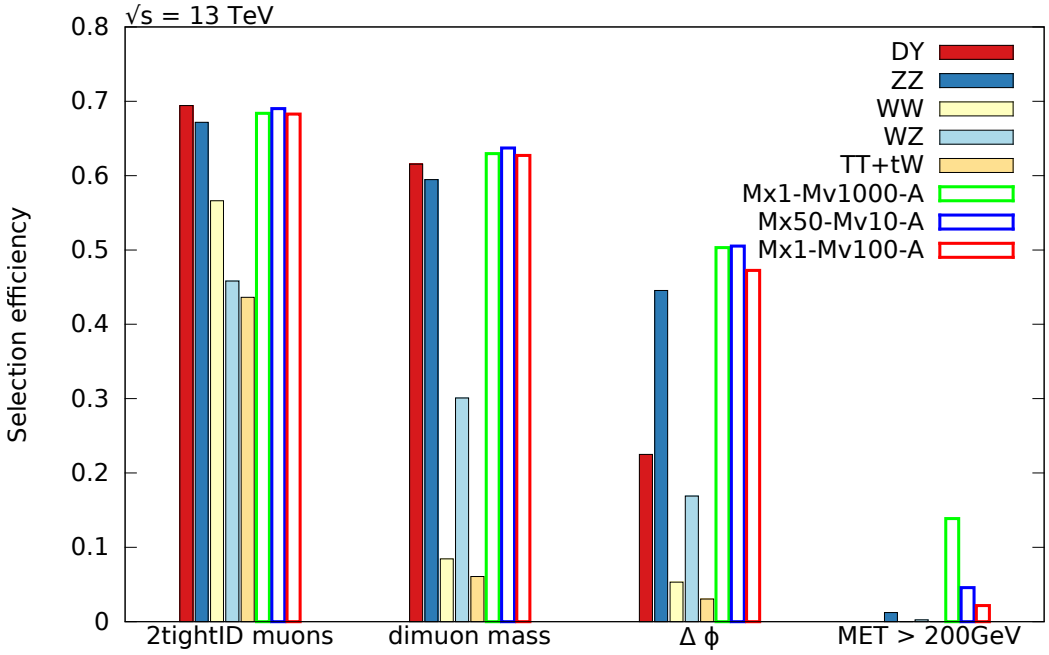

Figure 2.5: Selection efficiencies (number of events after applied selection criteria divided by number of triggered events) for the different applied requirement stages in the order from left to right. The selection of the dimuon masses reduces the WW, top quark pair and single top quark background significantly, while the selection on the angle between MET and dimuon pair reduces the Drell-Yan background significantly. The benchmark signals as well as the irreducible ZZ background are much less effected by the selection. The signal region with a MET threshold of 200 GeV is dominated by the signal.

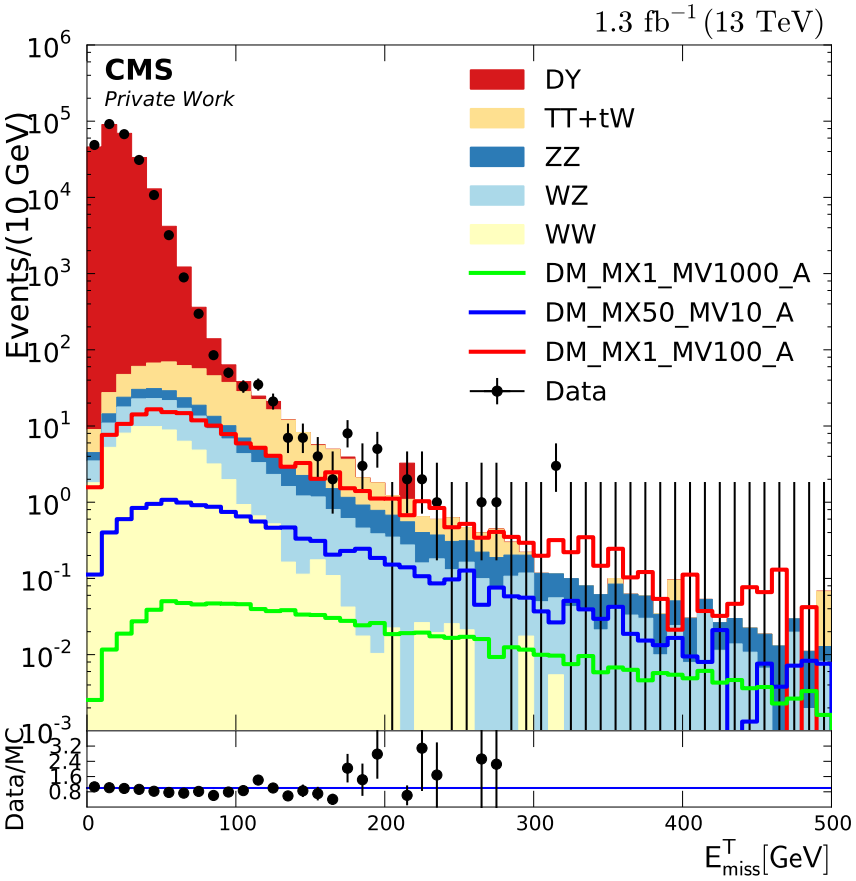

Figure 2.6: Missing transverse energy distribution after the final selection with exemplary dark matter signals. No significant deviation from the standard model prediction is observed.

unclustered MET [1] have to be taken into account, so they are all estimated for the signal regions. The further analysis is based on the number of Monte Carlo simulated events after applying the selection criteria in the signal regions N, so the systematic uncertainties on this number of events is estimated. This is performed as follows.

For every event, the momentum of each particle type (muon, electron, jet, unclustered MET and tau) is shifted within its uncertainties up or down, and the MET is recalculated using these shifted momentum. This creates for every available particle and every available systematic uncertainty source (resolution or scale uncertainty) two new events, one with the momenta shifted up, and one with the momenta shifted down. For these colloquially referred to as shifted events, the selection steps are applied and then the number of events in the signal region N_{up} and N_{down} are each counted for every systematic uncertainty source and particle. Then, to estimate the uncertainties on the number of events N in the signal regions,

$$\sigma_N = \frac{|N_{\text{up}} - N_{\text{down}}|}{N} \tag{2.3}$$

is calculated for every systematic uncertainty source and particle, and signal region. These different σ_N are then combined to the total systematic uncertainty on the number of events for different MET thresholds.

These shiftings are implemented in TAPAS, for further information see [42].

The resulting relative systematic uncertainties on the event numbers for different signal regions caused by these shifted particle momenta can be found in table 2.4. Additionally to that, there is a systematic uncertainty on the luminosity of 12% [50].

There are systematic uncertainties which could not be considered in terms of the current thesis, for example the parton distribution function uncertainty.

[1] The unclustered MET is the MET measured in the calorimeters without the MET caused by the reconstructed particles.

particle and shifttype	rel. uncertainty
muon resolution	0.5 - 2%
muon scale	0.7 - 2%
electron scale	$< 0.01\%$
jet scale	0.1 - 4%
jet resolution	0.1 - 0.9%
tau scale	6 - 9%
MET unclustered scale	1 - 4%

Table 2.4: Relative uncertainties on the number of events after selection and above the different MET thresholds (signal regions) N due to uncertainties (resolution or scale) of different groups of particles. These uncertainties are calculated using (2.3) for the different Monte Carlo background samples, and then combined to the total uncertainty. The uncertainties depend on the MET threshold, so the minimum and maximum relative uncertainty are shown here.

Chapter 3

Results and statistical interpretation

3.1 Single bin evaluation

After the final selection, the number of standard model background events with systematical uncertainty, and the number of observed events (see table 3.1) in the signal regions are counted.

The signal regions are above different MET thresholds, denoted as $\mathrm{MET}_{>}$. Since there is no significant excess of data, model-independent limits on the cross section for beyond standard model events in the Z+MET channel for the different $\mathrm{MET}_{>}$ (similar to [28]), and limits on the mass of mediator and dark matter particle χ are calculated.

The 95% CL expected upper limit signal strength parameter μ, given by

$$\mu = \frac{\text{number of signal events}}{\text{number of exp. signal events}}, \tag{3.1}$$

as well as the 1σ, the 2σ band and the observed limit are calculated using the CMSSW tool 'Higgs Combine' [51]. For this analysis, the asymptotic CL_s method [52] is used.

The number of background events and the number of expected signal events are the input parameters for the Higgs Combine tool. If one sets the number of expected signal events to 1, (3.1) becomes

$$\mu = \text{number of signal events} = \mathscr{L}_{\mathrm{int}} \epsilon A \sigma, \tag{3.2}$$

with the integrated luminosity $\mathscr{L}_{\mathrm{int}}$, the detector acceptance A, the selection efficiency ϵ, and the cross section σ for the process corresponding to the number of events.

Since μ is the upper limit for the predicted event count within the standard model backgrounds uncertainties, the upper limit for cross sections covered in the standard model expectation can be calculated via (3.2).

$MET_{>}$	120 GeV	140 GeV	160 GeV	180 GeV	200 GeV	220 GeV
MC samples	number of events					
$t\bar{t}$	39.39 ± 9.42	19.53 ± 5.84	10.29 ± 3.87	4.52 ± 2.29	2.68 ± 1.74	1.60 ± 1.33
WZ	9.42 ± 3.52	6.18 ± 2.78	4.09 ± 2.20	2.83 ± 1.78	2.01 ± 1.47	1.41 ± 1.22
ZZ	9.33 ± 3.46	6.39 ± 2.78	4.51 ± 2.29	3.26 ± 1.91	2.40 ± 1.62	1.79 ± 1.39
DY-M50	7.21 ± 5.44	2.51 ± 1.62	2.42 ± 1.58	2.17 ± 1.50	2.17 ± 1.50	0.00 ± 0.00
s-antitop	1.37 ± 1.21	0.42 ± 0.66	0.26 ± 0.59	0.09 ± 0.30	0.00 ± 0.00	0.00 ± 0.00
WW	1.29 ± 1.18	0.61 ± 0.79	0.32 ± 0.58	0.17 ± 0.41	0.14 ± 0.38	0.12 ± 0.35
s-top	1.04 ± 1.08	0.42 ± 0.66	0.26 ± 0.51	0.26 ± 0.52	0.00 ± 0.00	0.00 ± 0.00
total bg	69.05 ± 16.97	36.06 ± 9.22	22.16 ± 6.48	13.29 ± 4.27	9.40 ± 3.48	4.92 ± 2.48
data	66	32	22	18	12	10

Table 3.1: Numbers of events in the signal regions, namely with MET greater than 120, 140, 160, 180, 200 and 220 GeV. The total uncertainty on the final event yield is the combined systematical and statistical uncertainty for the corresponding MET threshold.

$MET_{>}$	observed	-2σ	-1σ	exp. mean	$+1\sigma$	$+2\sigma$
120 GeV	26.40	15.73	20.57	27.88	37.99	49.50
140 GeV	13.88	8.76	11.66	16.19	22.83	30.77
160 GeV	12.42	6.65	8.94	12.56	17.82	24.43
180 GeV	13.79	5.05	6.83	9.75	14.14	19.78
200 GeV	10.30	4.06	5.54	8.03	11.78	16.77
220 GeV	11.53	3.17	4.36	6.41	9.60	13.96

Table 3.2: Signal strength parameter μ which is calculated by the Higgs Combine tool within the asymptotic CL_s method.

3.2 Model independent limits

To calculate the model independent upper limit on cross sections for standard model events with the Z+MET signature and different MET thresholds $\sigma^{\mathrm{BSM}}(\mathrm{MET}_{>})$, the signal strength parameter μ is computed for these different MET thresholds.

The results can be found in table 3.2. With these μ, the upper limit on $\sigma^{\mathrm{BSM}}(\mathrm{MET}_{>})$ can be calculated by plugging

$$A\epsilon = \frac{N_{\text{after selection}}}{N_{\text{gen}}} \tag{3.3}$$

into (3.2). This $A\epsilon$ is calculated for every available dark matter signal, since the dark matter signals are used as benchmark events for this Z+MET channel. Based on these calculations, the detector acceptance A times selection efficiency ϵ is estimated to be 17%. In summary, the upper limits for $\sigma^{\mathrm{BSM}}(\mathrm{MET}_{>})$ are

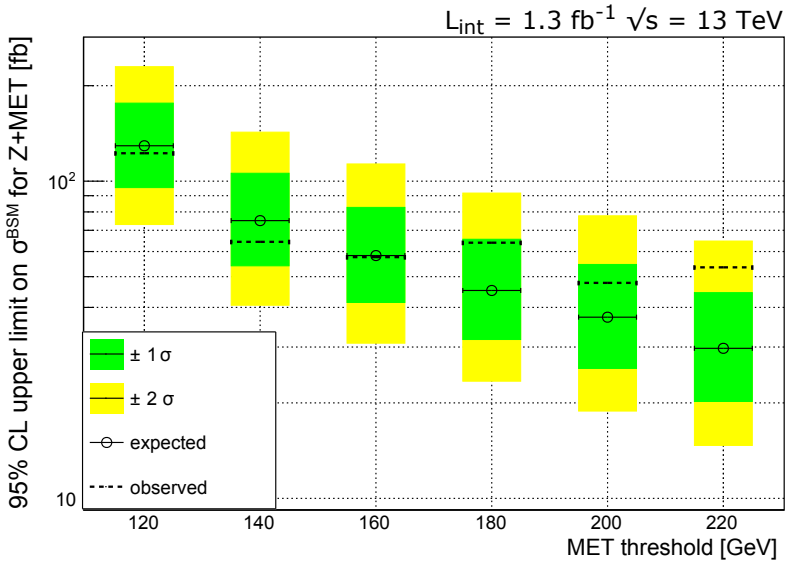

Figure 3.1: Limits on cross sections for beyond standard model processes depending on different missing transverse energy thresholds for the Z+MET channel. The observed limit is denoted with the dashed line.

given by

$$\sigma^{\mathrm{BSM}}(\mathrm{MET}_{>}) = \frac{\mu(\mathrm{MET}_{>})}{A\epsilon\mathscr{L}_{\mathrm{int}}}. \tag{3.4}$$

fig. 3.1 shows the results of this computation.

These limits can be interpreted in a way that they give an upper limit on cross sections for beyond standard model processes with a Z boson that decays into two muons, and missing transverse energy. Thus, if there are models with comparable efficiency and channel, one can estimate limits for these models using the number of signal events after selection and above MET threshold $N_{\mathrm{sel},>}$, and the number of signal events after selection N_{sel} by

$$\sigma^{\mathrm{Model}} = \sigma^{\mathrm{BSM}}(\mathrm{MET}_{>})\frac{N_{\mathrm{sel},>}}{N_{\mathrm{sel}}}. \tag{3.5}$$

In the following, model-dependent limits will be calculated. Since the detector acceptance A times selection efficiency ϵ was only an estimate, the efficiency for every signal will be determined to calculate the upper limit on σ_{DM}, therefore, this above described method will not be used.

coupling	M_{med}	excluded M_χ [GeV]
A	10 GeV	$\leq$ 2.5 GeV
V	10 GeV	$\leq$ 1.1 GeV
coupling	M_χ	excluded M_{med}
A	1 GeV	$\leq$ 12 GeV
V	1 GeV	$\leq$ 30 GeV

Table 3.3: At 95% CL excluded dark matter production scenarios based on the limit calculations in section 3.3.

3.3 Limits on the dark matter and mediator mass

To estimate the limits on the production cross section σ_{DM} in dependence of different models for dark matter, i.e. different mediator masses, different dark matter particle masses and for axial-vector or vector coupling, the signal strength parameter μ is used again to calculate

$$\sigma_{\mathrm{DM}} = \frac{\mu}{\mathscr{L}_{\mathrm{int}} A\epsilon_{>}}. \tag{3.6}$$

The signal region is determined to be at MET > 200 GeV.

This time, the cross section σ_{DM} does not depend on a certain MET threshold, it is the cross section for the overall production. Thus, the efficiency must now contain the requirement of the events to have MET > 200 GeV. Using the total number of signal events after selection and above MET threshold $N_{\mathrm{sel},>}$, and the total number of generated Monte Carlo signal N_{gen}, the efficiency is given by

$$A\epsilon = \frac{N_{\mathrm{sel},>}}{N_{\mathrm{gen}}}. \tag{3.7}$$

Using that relation, upper limits on cross sections for the different models of dark matter production are obtained. The efficiencies are given in table 5.1 and table 5.2 in the appendix.

One has to mention that this is an estimate since there are no uncertainties on $N_{\mathrm{sel},>}$ regarded, only systematic uncertainties on the background events are taken into account.

The results of this computation can be found in fig. 3.2 - fig. 3.7. Based on these, one can exclude the dark matter models with mediator mass $M_{\mathrm{med}} =$ 10 GeV and dark matter mass $M_\chi \leq 2.5$ (1.1) GeV for axial-vector (vector) coupling, and with dark matter mass $M_\chi =$1 GeV and mediator mass $M_{\mathrm{med}} \leq 12$ (30) GeV for axial-vector (vector) coupling, since the predicted cross sections of these models are higher than the observed upper limit. These exclusions are summarized in table 3.3.

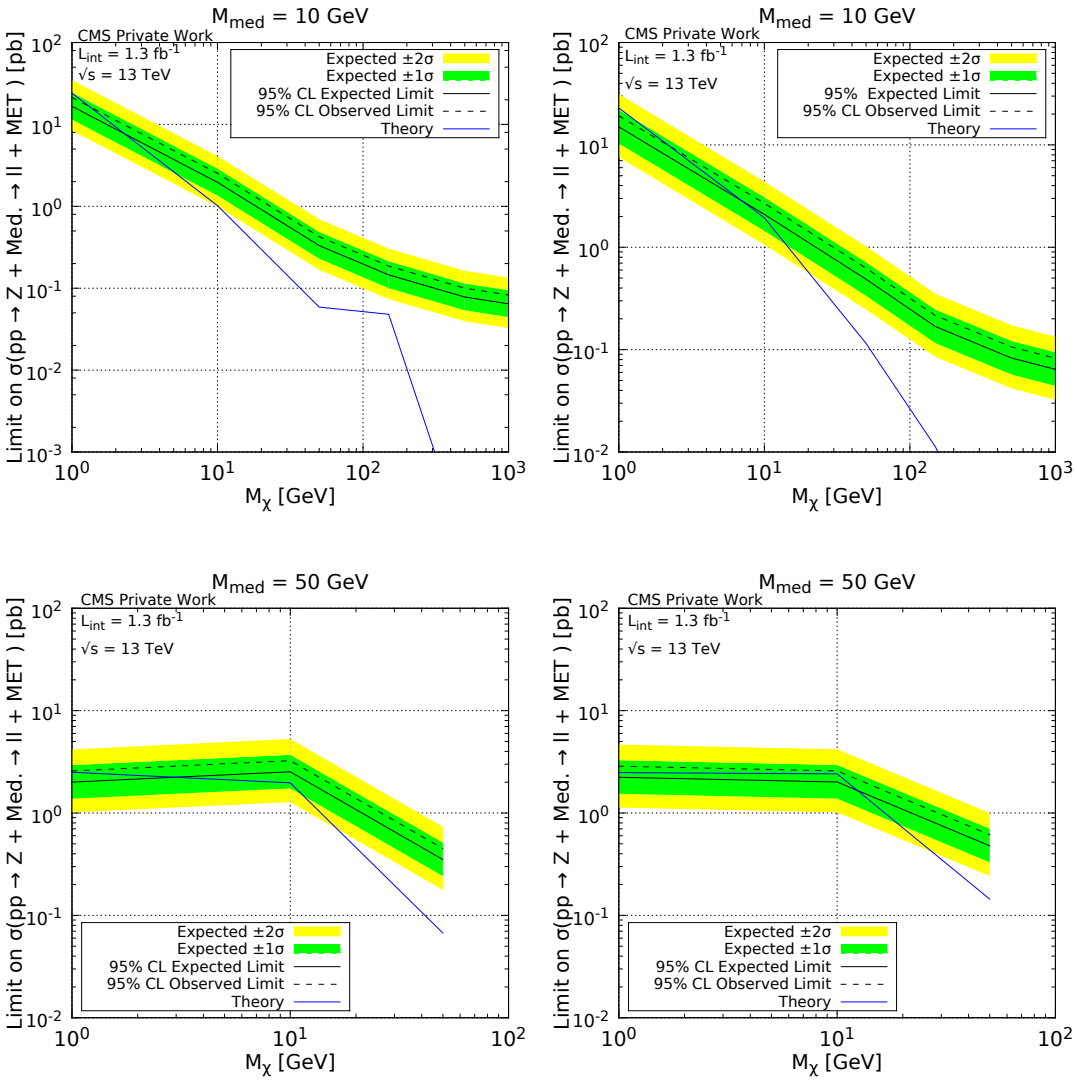

Figure 3.2: Upper limit on the cross section in dependence of the dark matter particle mass M_χ for mediator masses $M_{\text{med}} = 10\,\text{GeV}$ (top) and 50 GeV (bottom). The pictures on the left show the axial-vector coupling, and on the right the vector coupling. The $\pm 1\sigma$ and $\pm 2\sigma$ band for the expected upper limit are also shown, as well as the observed limit as dashed line. The theoretical production cross section is shown. The scenarios with production cross section above the observed upper limit are excluded at 95% confidence level.

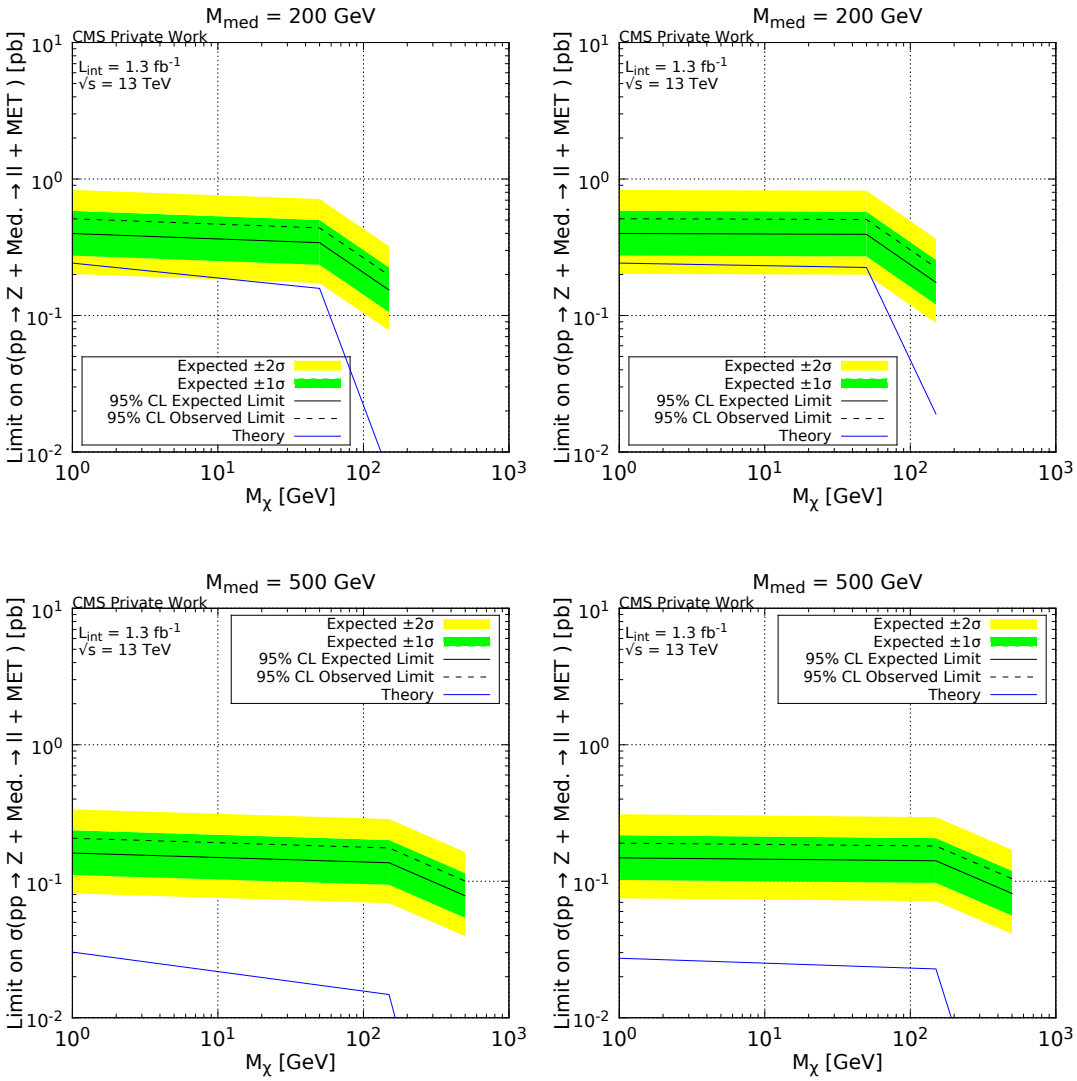

Figure 3.3: Upper limit on the cross section in dependence of the dark matter particle mass M_χ for mediator masses $M_{\text{med}} = 200\,\text{GeV}$ (top) and $500\,\text{GeV}$ (bottom). The pictures on the left show the axial-vector coupling, and on the right the vector coupling. The $\pm1\sigma$ and $\pm2\sigma$ band for the expected upper limit are also shown, as well as the observed limit as dashed line. The theoretical production cross section is shown. The scenarios with production cross section above the observed upper limit are excluded at 95% confidence level.

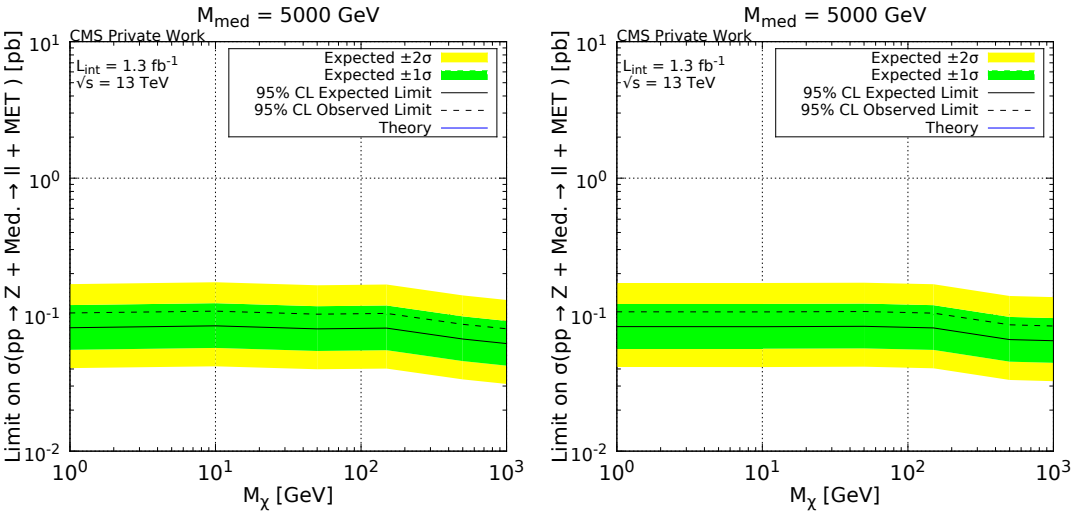

Figure 3.4: Upper limit on the cross section in dependence of the dark matter particle mass M_χ for a mediator mass $M_{\text{med}} = 5000\,\text{GeV}$. The picture on the left shows the axial-vector coupling, and on the right the vector coupling. The $\pm 1\sigma$ and $\pm 2\sigma$ band for the expected upper limit are also shown, as well as the observed limit as dashed line. The theoretical production cross section for these scenarios is smaller than 10^{-2} pb and therefore not shown, compare fig. 1.6.

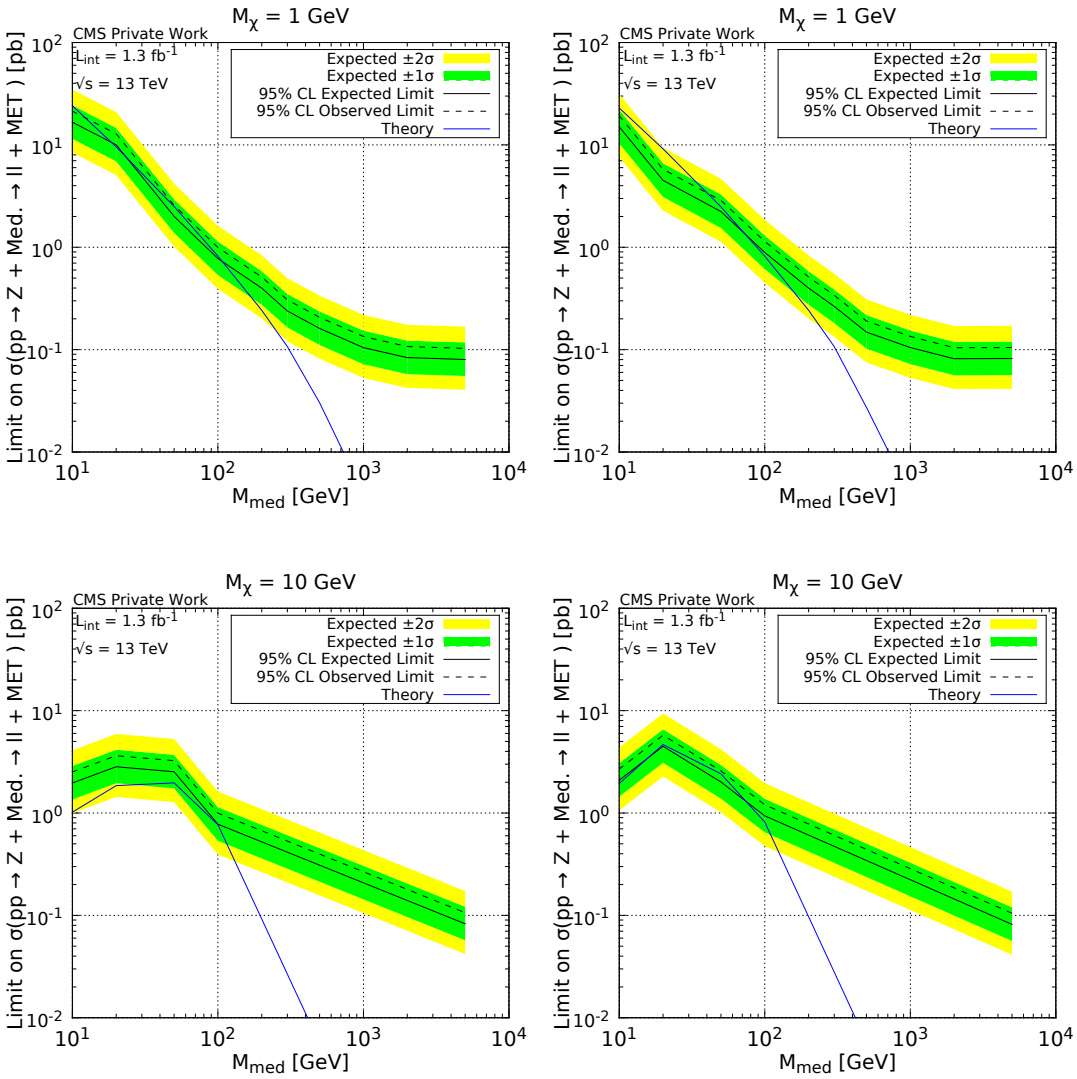

Figure 3.5: Upper limit on the cross section in dependence of the mediator mass M_{med} for the dark matter masses $M_\chi = 1\,\text{GeV}$ (top) and $10\,\text{GeV}$ (bottom). The pictures on the left show the axial-vector coupling, and on the right the vector coupling. The $\pm1\sigma$ and $\pm2\sigma$ band for the expected upper limit are also shown, as well as the observed limit as dashed line. The theoretical production cross section is shown. The scenarios with production cross section above the observed upper limit are excluded at 95% confidence level.

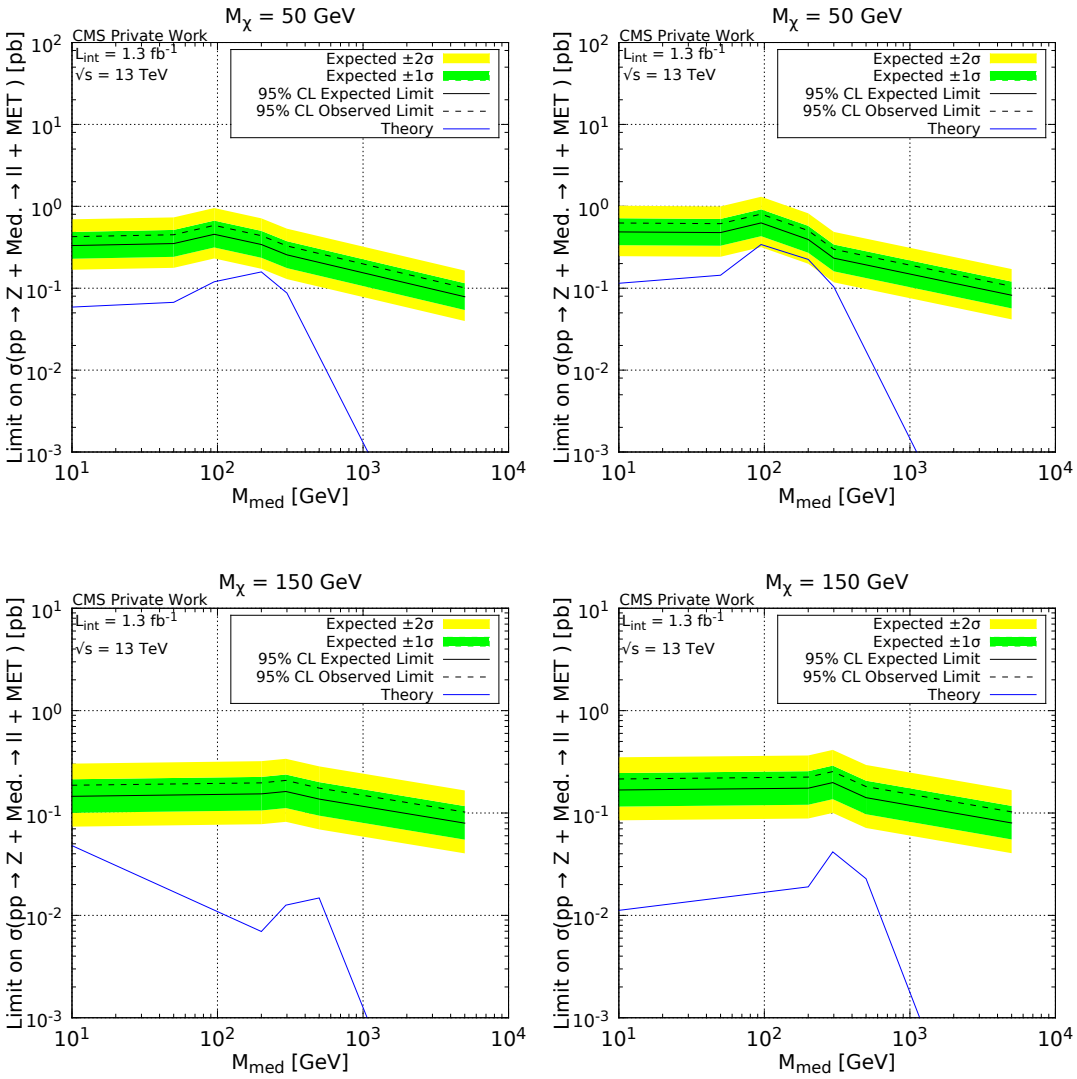

Figure 3.6: Upper limit on the cross section in dependence of the mediator mass M_{med} for the dark matter masses $M_\chi = 50\,\text{GeV}$ (top) and 150 GeV (bottom). The pictures on the left show the axial-vector coupling, and on the right the vector coupling. The $\pm 1\sigma$ and $\pm 2\sigma$ band for the expected upper limit are also shown, as well as the observed limit as dashed line. The theoretical production cross section is shown. The scenarios with production cross section above the observed upper limit are excluded at 95% confidence level.

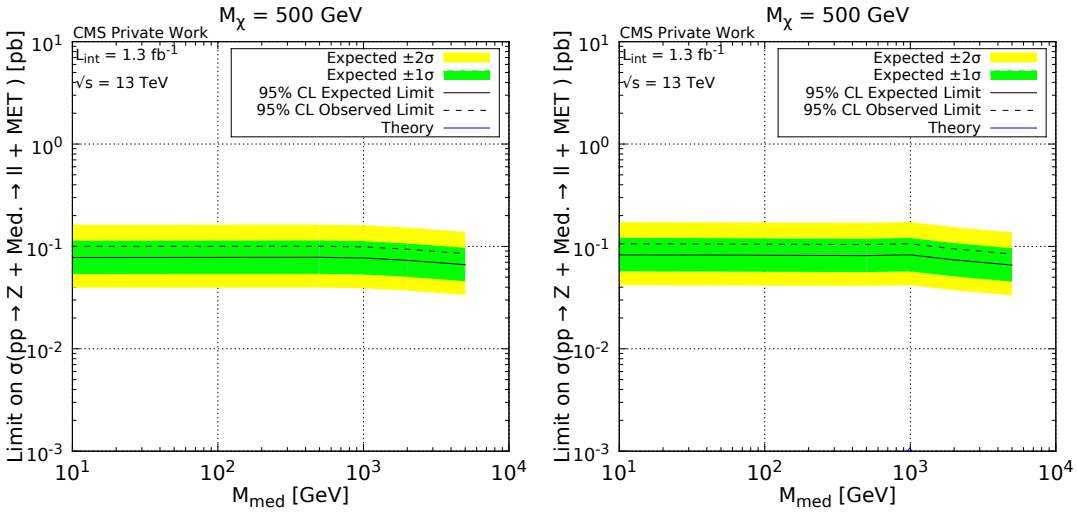

Figure 3.7: Upper limit on the cross section in dependence of the mediator mass M_{med} for the dark matter mass $M_\chi = 500\,\text{GeV}$. The picture on the left shows the axial-vector coupling, and on the right the vector coupling. The $\pm 1\sigma$ and $\pm 2\sigma$ band for the expected upper limit are also shown, as well as the observed limit as dashed line. The theoretical production cross section for these scenarios is smaller than 10^{-3} pb and therefore not shown, compare fig. 1.6.

Chapter 4

Summary

In this work, the Z+MET channel for dark matter production is investigated. The properties of the production channel are described. Based on these, standard model backgrounds are considered and selection requirements on both simulated and data events are applied to reduce the background and achieve a good signal sensitivity.

The final missing transverse energy distribution is used to calculate model-independent, as well as model-dependent upper limits on cross sections.

For the model-independent limits, upper limits on cross sections for beyond standard model processes are calculated in dependence of different missing transverse energy thresholds.

The signal region is determined to be above a MET threshold of 200 GeV, and thus this additional requirement on data and simulation is used to calculate model-dependent limits on the production cross sections. These calculations are performed for different dark matter scenarios, depending on mediator mass, dark matter particle mass, and mediator coupling to the dark matter particles. Comparing these limits to the cross sections given by the model scenario, for four scenarios different theory parameters can be excluded.

This analysis provides a first look into the new LHC RunII data in the Z+MET dark matter production channel. Even with an integrated luminosity of $1.3\,\mathrm{fb}^{-1}$, which is about ten times lower than in RunI, four scenarios for different dark matter productions could be excluded at 95% CL which shows the sensitivity of the LHC and CMS detector to these dark matter models. With more data in the next year, these sensitivity will increase and hopefully bring new insights to particle dark matter.

Chapter 5

Appendix

M_{med} [GeV]	M_χ [GeV]					
	1	10	50	150	500	1000
10	$3.807{\cdot}10^{-4}$	$3.225{\cdot}10^{-3}$	$1.907{\cdot}10^{-2}$	$4.351{\cdot}10^{-2}$	$8.124{\cdot}10^{-2}$	$9.830{\cdot}10^{-2}$
20	$6.326{\cdot}10^{-4}$	$2.236{\cdot}10^{-3}$	-	-	-	-
50	$3.159{\cdot}10^{-3}$	$2.506{\cdot}10^{-3}$	$1.806{\cdot}10^{-2}$	-	-	-
95	-	-	$1.389{\cdot}10^{-2}$	-	-	-
100	$8.160{\cdot}10^{-3}$	$8.146{\cdot}10^{-3}$	-	-	-	-
200	$1.588{\cdot}10^{-2}$	-	$1.854{\cdot}10^{-2}$	$4.122{\cdot}10^{-2}$	-	-
295	-	-	-	$3.906{\cdot}10^{-2}$	-	-
300	$2.653{\cdot}10^{-2}$	-	$2.478{\cdot}10^{-2}$	-	-	-
500	$3.930{\cdot}10^{-2}$	-	-	$4.634{\cdot}10^{-2}$	$8.094{\cdot}10^{-2}$	-
995	-	-	-	-	$8.217{\cdot}10^{-2}$	-
1000	$6.056{\cdot}10^{-2}$	-	-	-	-	$9.969{\cdot}10^{-2}$
1995	-	-	-	-	-	$9.730{\cdot}10^{-2}$
2000	$7.581{\cdot}10^{-2}$	-	-	-	$8.656{\cdot}10^{-2}$	-
5000	$7.900{\cdot}10^{-2}$	$7.653{\cdot}10^{-2}$	$8.054{\cdot}10^{-2}$	$7.953{\cdot}10^{-2}$	$9.557{\cdot}10^{-2}$	1.031e-01

Table 5.1: Efficiencies $A\epsilon = (N_{\text{sel},>})/(N_{\text{gen}})$ (see section 3.3) for axial-vector coupling. The combinations denoted by a bar are not available.

M_{med} [GeV]	M_χ [GeV]					
	1	10	50	150	500	1000
10	$4.226 \cdot 10^{-4}$	$3.021 \cdot 10^{-3}$	$1.300 \cdot 10^{-2}$	$3.776 \cdot 10^{-2}$	$7.655 \cdot 10^{-2}$	$9.870 \cdot 10^{-2}$
20	$1.406 \cdot 10^{-3}$	$1.411 \cdot 10^{-3}$	-	-	-	-
50	$2.835 \cdot 10^{-3}$	$3.154 \cdot 10^{-3}$	$1.324 \cdot 10^{-2}$	-	-	-
95	-	-	$1.010 \cdot 10^{-2}$	-	-	-
100	$7.122 \cdot 10^{-3}$	$6.748 \cdot 10^{-3}$	-	-	-	-
200	$1.588 \cdot 10^{-2}$	-	$1.609 \cdot 10^{-2}$	$3.625 \cdot 10^{-2}$	-	-
295	-	-	-	$3.197 \cdot 10^{-2}$	-	-
300	$2.397 \cdot 10^{-2}$	-	$2.718 \cdot 10^{-2}$	-	-	-
500	$4.270 \cdot 10^{-2}$	-	-	$4.484 \cdot 10^{-2}$	$7.787 \cdot 10^{-2}$	-
995	-	-	-	-	$7.660 \cdot 10^{-2}$	-
1000	$6.042 \cdot 10^{-2}$	-	-	-	-	$9.648 \cdot 10^{-2}$
1995	-	-	-	-	-	$9.734 \cdot 10^{-2}$
2000	$7.780 \cdot 10^{-2}$	-	-	-	$8.579 \cdot 10^{-2}$	-
5000	$7.746 \cdot 10^{-2}$	$7.756 \cdot 10^{-2}$	$7.708 \cdot 10^{-2}$	$7.917 \cdot 10^{-2}$	$9.646 \cdot 10^{-2}$	$9.837 \cdot 10^{-2}$

Table 5.2: Efficiencies $A\epsilon = (N_{\text{sel},>})/(N_{\text{gen}})$ (see section 3.3) for vector coupling. The combinations denoted by a bar are not available.

Danksagung

An dieser Stelle möchte ich mich herzlich bei Herrn Professor Hebbeker dafür bedanken, dass ich diese Bachelorarbeit schreiben durfte und mir die Möglichkeit gegeben wurde, mit echten Daten vom LHC zu arbeiten - das hätte ich vor ein paar Monaten nicht für möglich gehalten.

Danke an Herrn Professor Wiebusch, der sich bereit erklärt hat, diese Arbeit als Zweitgutachter zu bewerten.

Danke an alle Mitglieder des Instituts IIIa. Die Herzlichkeit, mit der ich aufgenommen wurde, ist genauso wenig selbstverständlich wie die Geduld, die mir bei den vielen Fragen, die ich gestellt habe, entgegengebracht wurde.

Insbesondere möchte ich Michael Brodski herzlich für die Betreuung und das Korrekturlesen meiner Arbeit danken.

Ich danke auch meinen Freunden und meiner Familie, die mich nicht nur in dieser Bachelorarbeitszeit sehr unterstützt haben.

Bibliography

[1] V. Luković, P. Cabella, and N. Vittorio, "Dark matter in cosmology", *International Journal of Modern Physics A* 29 (2014), no. 19, 1443001. doi:10.1142/s0217751x14430015.

[2] F. Zwicky, "Die Rotverschiebung von extragalaktischen Nebeln", *Helvetica Physica Acta* 6 (1933) 110–127.

[3] V. C. Rubin, N. Thonnard, and J. F. W. K., "Rotational properties of 21 SC galaxies with a large range of luminosities and radii, from NGC 4605 /R = 4kpc/ to UGC 2885 /R = 122 kpc/", *ApJ* 238 (1980) 471. doi:10.1086/158003.

[4] http://www.physikblog.eu/wp-content/uploads/2011/05/Rotationskurve.png. Rotational velocity graph.

[5] http://cdn.phys.org/newman/gfx/news/hires/2013/4-3-2-1-gravitationa.jpg. Gravitational lensing sketch.

[6] M. Bartelmann and P. Schneider, "Weak gravitational lensing", *Phys. Rept.* 340 (2001) 291–472, arXiv:astro-ph/9912508. doi:10.1016/S0370-1573(00)00082-X.

[7] http://apod.nasa.gov/apod/image/0608/bulletcluster_comp_f2048.jpg. Picture of a weak gravitational lensing effect.

[8] http://apod.nasa.gov/apod/image/1112/lensshoe_hubble_3235.jpg. Picture of a strong gravitational lensing effect.

[9] D. Fabricant, M. Lecar, and P. Gorenstein, "X-ray measurements of the mass of M87", *ApJ* 241 (1980) 552. doi:10.1086/158369.

[10] T. Matilsky, C. Jones, and W. Forman, "An X-ray study of the Centaurus Cluster of galaxies using Einstein", *ApJ* 291 (April, 1985) 621–626. doi:10.1086/163102.

[11] L. P. David, C. Jones, W. Forman et al., "Mapping the dark matter in the NGC 5044 group with ROSAT: Evidence for a nearly homogeneous cooling flow with a cooling wake", *ApJ* 428 (June, 1994) 544–554. doi:10.1086/174264.

[12] C. Jones, C. Stern, W. Forman et al., "X-Ray Emission from the Fornax Cluster", *ApJ* 482 (June, 1997) 143–155.

[13] E. Komatsu, K. M. Smith, J. Dunkley et al., "SEVEN-YEAR WILKINSON MICROWAVE ANISOTROPY PROBE (WMAP) OBSERVATIONS: COSMOLOGICAL INTERPRETATION", *ApJS* 192 (2011), no. 2, 18. doi:10.1088/0067-0049/192/2/18.

[14] http://www.physik.uzh.ch/groups/serra/images/SM1.png. Standard model collection scheme.

[15] CMS Collaboration, "Observation of a new boson at a mass of 125 GeV with the CMS experiment at the LHC", *Phys. Lett.* B716 (2012) 30–61, arXiv:1207.7235. doi:10.1016/j.physletb.2012.08.021.

[16] G. Bertone, D. Hooper, and J. Silk, "Particle dark matter: evidence, candidates and constraints", *Physics Reports* 405 (2005), no. 5-6, 279–390. doi:10.1016/j.physrep.2004.08.031.

[17] The Fermi-LAT Collaboration Collaboration, "Constraining Dark Matter Models from a Combined Analysis of Milky Way Satellites with the Fermi Large Area Telescope", *Phys. Rev. Lett.* 107 (Dec, 2011) 241302. doi:10.1103/PhysRevLett.107.241302.

[18] J. Buckley et al., "Working Group Report: WIMP Dark Matter Indirect Detection", in *Community Summer Study 2013: Snowmass on the Mississippi (CSS2013) Minneapolis, MN, USA, July 29-August 6, 2013.* 2013. arXiv:1310.7040.

[19] LUX Collaboration, "First results from the LUX dark matter experiment at the Sanford Underground Research Facility", *Phys. Rev. Lett.* 112 (2014) 091303, arXiv:1310.8214. doi:10.1103/PhysRevLett.112.091303.

[20] IceCube Collaboration, "Multi-year search for dark matter annihilations in the Sun with the AMANDA-II and IceCube detectors", *Phys. Rev.* D85 (2012) 042002, arXiv:1112.1840. doi:10.1103/PhysRevD.85.042002.

[21] PICASSO Collaboration, "Constraints on Low-Mass WIMP Interactions on ^{19}F from PICASSO", *Phys. Lett.* B711 (2012) 153–161, arXiv:1202.1240. doi:10.1016/j.physletb.2012.03.078.

[22] CMS Collaboration, "Search for dark matter, extra dimensions, and unparticles in monojet events in proton–proton collisions at $\sqrt{s} = 8$ TeV", *Eur. Phys. J.* C75 (2015), no. 5, 235, arXiv:1408.3583. doi:10.1140/epjc/s10052-015-3451-4.

[23] ATLAS Collaboration, "Search for new phenomena in final states with an energetic jet and large missing transverse momentum in pp collisions at $\sqrt{s}$ =8 TeV with the ATLAS detector", *Eur. Phys. J.* C75 (2015), no. 7, 299, arXiv:1502.01518. [Erratum: Eur. Phys. J.C75,no.9,408(2015)]. doi:10.1140/epjc/s10052-015-3517-3, 10.1140/epjc/s10052-015-3639-7.

[24] ATLAS Collaboration, "Search for new phenomena in events with a photon and missing transverse momentum in *pp* collisions at $\sqrt{s} = 8$ TeV with the ATLAS detector", *Phys. Rev.* D91 (2015), no. 1, 012008, arXiv:1411.1559. [Erratum: Phys. Rev.D92,no.5,059903(2015)]. doi:10.1103/PhysRevD.92.059903, 10.1103/PhysRevD.91.012008.

[25] CMS Collaboration, "Search for physics beyond the standard model in final states with a lepton and missing transverse energy in proton-proton collisions at sqrt(s) = 8 TeV", *Phys. Rev.* D91 (2015), no. 9, 092005, arXiv:1408.2745. doi:10.1103/PhysRevD.91.092005.

[26] ATLAS Collaboration, "Search for dark matter in events with heavy quarks and missing transverse momentum in *pp* collisions with the ATLAS detector", *Eur. Phys. J.* C75 (2015), no. 2, 92, arXiv:1410.4031. doi:10.1140/epjc/s10052-015-3306-z.

[27] D. Alves, N. Arkani-Hamed, S. Arora et al., "Simplified models for LHC new physics searches", *Journal of Physics G: Nuclear and Particle Physics* 39 (2012), no. 10, 105005. doi:10.1088/0954-3899/39/10/105005.

[28] CMS Collaboration, "Search for dark matter and unparticles produced in association with a Z boson in proton-proton collisions at sqrt(s) = 8 TeV", arXiv:1511.09375.

[29] O. Buchmueller, M. J. Dolan, and C. McCabe, "Beyond Effective Field Theory for Dark Matter Searches at the LHC", *JHEP* 01 (2014) 025, arXiv:1308.6799. doi:10.1007/JHEP01(2014)025.

[30] L. Evans and P. Bryant, "LHC Machine", *Journal of Instrumentation* 3 (2008), no. 08, S08001.

[31] http://diversity.web.cern.ch/scope/nationality-and-culture. Information about people working at CERN, accessed on 07.12.15.

[32] LHCb Collaboration, "The LHCb Detector at the LHC", *Journal of Instrumentation* 3 (2008), no. 08, S08005.

[33] ALICE Collaboration, "The ALICE experiment at the CERN LHC", *Journal of Instrumentation* 3 (2008), no. 08, S08002.

[34] ATLAS Collaboration, "Measurement of the Inelastic Proton-Proton Cross Section at $\sqrt{s} = 13$ TeV with the ATLAS Detector at the LHC",.

[35] CMS Collaboration, "The CMS experiment at the CERN LHC", *Journal of Instrumentation* 3 (2008), no. 08, S08004.

[36] `https://inspirehep.net/record/884672/files/cms.png`. CMS sketch.

[37] CMS Collaboration, "Performance of Photon Reconstruction and Identification with the CMS Detector in Proton-Proton Collisions at sqrt(s) = 8 TeV", *JINST* 10 (2015), no. 08, P08010, `arXiv:1502.02702`. `doi:10.1088/1748-0221/10/08/P08010`.

[38] `https://inspirehep.net/record/1251416/files/Figures_Experimental_Apparatus_MuonDetector.png`. Sketch of the muon detectors.

[39] J. Alwall, M. Herquet, F. Maltoni et al., "MadGraph 5 : Going Beyond", *JHEP* 06 (2011) 128, `arXiv:1106.0522`. `doi:10.1007/JHEP06(2011)128`.

[40] S. Frixione, P. Nason, and C. Oleari, "Matching NLO QCD computations with Parton Shower simulations: the POWHEG method", *JHEP* 11 (2007) 070, `arXiv:0709.2092`. `doi:10.1088/1126-6708/2007/11/070`.

[41] S. Agostinelli, J. Allison, K. Amako et al., "Geant4—a simulation toolkit", *Nuclear Instruments and Methods in Physics Research Section A: Accelerators, Spectrometers, Detectors and Associated Equipment* 506 (2003), no. 3, 250 – 303. `doi:http://dx.doi.org/10.1016/S0168-9002(03)01368-8`.

[42] `https://gitlab.cern.ch/aachen-3a/tapas`. 'Three A Physics Analysis Software', analysis framework on Github.

[43] `https://twiki.cern.ch/twiki/bin/view/CMSPublic/WorkBookCMSSWFramework`. The CMSSW framework, CMS Twiki.

[44] `https://twiki.cern.ch/twiki/bin/viewauth/CMS/SummaryTable1G25ns`. Summary of cross sections for different Monte Carlo samples, CMS Twiki, accessed on 20.12.15.

[45] https://twiki.cern.ch/twiki/bin/view/CMS/SWGuideMuonIdRun2. Definition of the tightID for muons for RunII, CMS Twiki.

[46] https://twiki.cern.ch/twiki/bin/view/CMS/SWGuideMuonIdRun2#Muon_Isolation. Particle flow isolation (pfIsoID) for muons, CMS Twiki.

[47] https://twiki.cern.ch/twiki/bin/viewauth/CMS/PileupJSONFileforData. CMSSW tool to create pileup distribution, CMS Twiki.

[48] https://twiki.cern.ch/twiki/bin/view/CMSPublic/WorkBookMetAnalysis. Corrections for MET, CMS Workbook.

[49] CMS Collaboration Collaboration, "Plans for Jet Energy Corrections at CMS", Technical Report CMS-PAS-JME-07-002, CERN, 2008. Geneva, 2008.

[50] https://indico.cern.ch/event/455330/session/0/contribution/176/attachments/1174516/1697270/CMSWeek_LumiReport.pdf. Luminosity report, CMS Week, accessed on 20.12.15.

[51] https://twiki.cern.ch/twiki/bin/viewauth/CMS/SWGuideHiggsAnalysisCombinedLimit. Higgs Combine tool of CMSSW, CMS Twiki.

[52] G. Cowan, K. Cranmer, E. Gross et al., "Asymptotic formulae for likelihood-based tests of new physics", *Eur. Phys. J. C* 71 (2011), no. 2, 1–19. doi:10.1140/epjc/s10052-011-1554-0.

Eidesstattliche Versicherung

Name, Vorname

Matrikelnummer (freiwillige Angabe)

Ich versichere hiermit an Eides Statt, dass ich die vorliegende Arbeit/Bachelorarbeit/ Masterarbeit* mit dem Titel

selbständig und ohne unzulässige fremde Hilfe erbracht habe. Ich habe keine anderen als die angegebenen Quellen und Hilfsmittel benutzt. Für den Fall, dass die Arbeit zusätzlich auf einem Datenträger eingereicht wird, erkläre ich, dass die schriftliche und die elektronische Form vollständig übereinstimmen. Die Arbeit hat in gleicher oder ähnlicher Form noch keiner Prüfungsbehörde vorgelegen.

Ort, Datum

Unterschrift

*Nichtzutreffendes bitte streichen

Belehrung:

§ 156 StGB: Falsche Versicherung an Eides Statt

Wer vor einer zur Abnahme einer Versicherung an Eides Statt zuständigen Behörde eine solche Versicherung falsch abgibt oder unter Berufung auf eine solche Versicherung falsch aussagt, wird mit Freiheitsstrafe bis zu drei Jahren oder mit Geldstrafe bestraft.

§ 161 StGB: Fahrlässiger Falscheid; fahrlässige falsche Versicherung an Eides Statt

(1) Wenn eine der in den §§ 154 bis 156 bezeichneten Handlungen aus Fahrlässigkeit begangen worden ist, so tritt Freiheitsstrafe bis zu einem Jahr oder Geldstrafe ein.

(2) Straflosigkeit tritt ein, wenn der Täter die falsche Angabe rechtzeitig berichtigt. Die Vorschriften des § 158 Abs. 2 und 3 gelten entsprechend.

Die vorstehende Belehrung habe ich zur Kenntnis genommen:

Ort, Datum

Unterschrift